Research Square

Preprints are preliminary reports that have not undergone peer review.
They should not be considered conclusive, used to inform clinical practice,
or referenced by the media as validated information.

Valorization of Palm-kernel Chaffs for Removal of Lead(II) from Water

Idowu J. Esho
Federal College of Education Special, Nigeria
Emmanuel F. Olasehinde
The Federal University of Technology
Matthew A. Adebayo
adebayoma@futa.edu.ng

The Federal University of Technology

Research Article

Keywords: Palm kernel chaffs, Valorization, Lead(II), Avrami model, Liu isotherm

Posted Date: September 2nd, 2026

DOI: https://doi.org/10.21203/rs.3.rs-10768761/v1

License: This work is licensed under a Creative Commons Attribution 4.0 International License.
Read Full License

Additional Declarations: No competing interests reported.

Valorization of Palm-kernel Chaffs for Removal of Lead(II) from Water

Idowu J. Esho[1,2], Emmanuel F. Olasehinde[1] and Matthew A. Adebayo[1,*]

[1]Department of Chemistry, The Federal University of Technology, Akure, Nigeria.

[2]Department of Chemistry, Federal College of Education (Special), Oyo, Nigeria.

*All correspondence to: adebayoma@futa.edu.ng (M.A. Adebayo)

Abstract

Heavy metal contamination including Pb^{2+} ions in water systems threatens environmental and public health, requiring the need for designing adsorbents that are affordable, eco-friendly, and effective. Biochars produced from agricultural biomass serve a potential roadmap for heavy metal remediation, but how sequential physical and chemical modifications of biochars control their adsorption behavior still limited; hence, systematic understanding persists. This present research assessed performances of three adsorbents {raw palm-kernel chaff (RPKC), physically pyrolyzed palm-kernel chaff (PPKC), and physically pyrolyzed–chemically activated palm-kernel chaff (CPPKC) using H_3PO_4 prepared from palm-kernel chaffs for removal of lead(II) ions from aqueous solutions. The adsorbents were characterized using FTIR, TGA, XRD, SEM–EDX, zeta potential, and BET surface area analysis. Batch adsorption experiments were performed to elucidate the effects of adsorbent dosage, pH, initial Pb^{2+} concentration, contact time, temperature on adsorption characteristics. Systematic analysis of adsorption kinetics, isotherms, and thermodynamics, using established models, was carried out. Pyrolysis and chemical activation progressively induced structural and chemical changes such as enhanced surface heterogeneity, increased porosity, and improved thermal stability. Adsorbent CPPKC exhibited the highest BET surface area 116.13 m^2/g, and pore volume 1.4327 cm^3/g, but lowest *PZC* (point of zero charge) of 5.19. Adsorption kinetics was best described by Avrami model while equilibrium data fitted into the Liu isotherm adequately. Highest Pb^{2+} removal of 6131.7 mg/g was exhibited by CPPKC. Thermodynamic analysis emphasized spontaneous and endothermic adsorption. This study justifies agricultural waste valorization as a feasible strategy for sustainable water treatment.

Keywords: Palm kernel chaffs, Valorization, Lead(II), Avrami model, Liu isotherm

1. Introduction

Lead (II) (Pb^{2+}) ion is one of the most toxic heavy metals in the environment. These metals are non-degradable, persistent, bio-accumulative toxic (Mititelu *et al.,* 2025; Xu *et al.,* 2024; Olasehinde *et al.,* 2019) and therefore, they constitute a global ecological problem. Lead (II) ions are not essential for soil, air, and water, and have no biological function (Mitra *et al.,* 2021). Health problems of environmental low level exposure to Pb^{2+} ions are neurological disorder, reproductive toxicity, cardiovascular disease, renal failure, anemia, renal and gastrointestinal disease, hematological disease and developmental problems in children (Mititelu *et al.,* 2025; Zhang *et al.,* 2023; Ashkan, 2023). Surface water in Africa and Asia contained lead concentrations above WHO guidelines for drinking water. The values of the hazard quotient index >1 indicated higher health risk on ingestion and dermal routes (Amit *et al.,* 2023).

The main sources of lead pollution in aquatic systems are human activities such as; battery production, mining, metal coating, dumping of industrial waste, metallurgical smelting and electronic waste (Adriana *et al.,* 2025; Adebayo *et al.,* 2012). The remediation of this metal is of major concern. The increase in lead concentration in environmental food chains has been attributed to natural, geographical and anthropogenic factors (Arowojobe *et al.,* 2021). These include pigment manufacturing, metal finishing, mine drainage, tannery operations, chemical and fertilizers production, leather production and leachates from contaminated groundwater (Aiyesanmi *et al.,* 2022; Olasehinde *et al.,* 2018). Conventional methods have been used for the extraction of Pb from the environment (Veer *et al.,* 2024; Aiyesanmi *et al.,* 2022; Aiyesanmi *et al.,* 2020; Olasehinde *et al.,* 2018). The main drawbacks of these conventional techniques are high operational cost, partial removal of pollutants, formation of toxic waste, general inefficiency and high energy consumption (Veer *et al.,* 2024; Ayach *et al.,* 2024). They have created one or more problems in their applications making it economically unattractive (Olasehinde *et al.,* 2018). However, these methods have their own drawbacks. For example, the membrane system is prone to fouling, scaling and clogging, while the ion exchange system is too expensive due to the cost of ion exchange resins (Aiyesanmi *et al.,* 2022). Hence, it is essential to develop a better, environmentally friendly, and sustainable method for environmental remediation.

The adsorption process has been used to remove the hazardous metals from the environmental water sources and it is proven to be economical, environmentally sustainable, user-friendly and highly effective (Fouda-Mbanga *et al.,* 2024). Adsorption is an ideal process for water treatment due to its versatility, high efficiency, simple operation and biocompatibility in environmental remediation in different conditions (Fouda-Mbanga *et al.,* 2024; Onyancha *et al.,* 2022). The adsorption technique is found to be very effective at minimum levels of pollutants, it is very simple to implement and the adsorbent used is recyclable. Thus, making the process reliable and efficient for environmental remediation.

The application of activated carbon as an adsorbent for the removal of pollutants has increased over the years but the high cost of production and recycling makes it unaffordable for large scale applications especially in the developing countries (Isaac *et al.,* 2024). Hence, agricultural biomass wastes and residues are used as alternative precursors for adsorbents production owing to their cost-effectiveness, availability and abundance (Kumar *et al.,* 2024). Biomass from different sources (agricultural wastes, forest by-products, aquatic plants, etc.) is sustainable, eco-friendly and can remediate potentially toxic metals as supported by several research works (Bhagya *et al.,* 2025). Pyrolysis of pistachio shells to biochar and chemically activated indicated 87 mg/g of CO2 adsorption strength (Alejandro *et al.,* 2025). The adsorptive efficiency of cyproflaxin using wheat straw based adsorbent was found to be 98% with maximum adsorption capacity 15.51 mg/g (Alawa *et al.,* 2025). Palm kernel chaffs (PKCs) are by-products of palm oil production industry which are commonly neglected or discarded leading to environmental pollution. Palm kernel shells are byproducts of the oil palm industry and a potential source of lignocellulosic biomass for the development of efficient adsorbent materials for environmental remediation. These substances are abundant in cellulose, hemicelluloses and lignin and have special physical and chemical properties which can be used for the removal of contaminants (Kuljit *et al.* 2024). Therefore, these materials are suitable for the preparation of efficient and effective adsorbents by valorization and surface modification. The environmentally sustainable properties of palm-kernel biomass in environmental remediation are not well investigated and its abundance especially in Nigeria has not been fully exploited in the production of efficient adsorbents. It is important to develop and improve the economical and efficient adsorbents based on palm-kernel chaffs for the removal of Pb^{2+} ions from aquatic ecosystems. The valorization of PKCs as an important agricultural waste can contribute to the circular economy goals, reduce

wastes, promote environmental sustainability and alleviate Pb(II) pollution. Therefore, the present study evaluates the enhancement of the PKCs *via* physical pyrolysis coupled with chemical activation by phosphoric acid (H_3PO_4) for removal of Pb^{2+} ions from simulated lead-contaminated aqueous systems, presenting a sustainable pathway to address the challenges of water purification and waste management.

2. Materials and Methodologies

The Merck Chemical Company of Germany provided all reagents utilized in this study, including phosphoric acid (H_3PO_4) with CAS number 7664-38-2, sodium hydroxide (NaOH) with CAS number 1310-73-2, Lead(II) nitrate ($Pb(NO_3)_2$), and Cadmium(II) nitrate ($Cd(NO_3)_2$). All chemicals were of analytical quality and required no additional purification.

2.1 Collection of Sample

The Palm-kernel Chaffs (PKCs) utilized as precursor material for this research were obtained from a supplier in Ilesa metropolis, Nigeria; botanical classification of the material was later conducted at the Department of Crop, Soil and Pest Management, Federal University of Technology, Akure, Nigeria.

2.2 Valorization of PKCs as Adsorbents and Characterisation

Powdered samples of the Raw Palm-kernel Chaffs (RPKCs) were produced *via* incessant grinding in a mortar and pestle, subsequently sieved using a 2 mm mesh, and then preserved in labeled, airtight containers for future application. To produce the pyrolysed adsorbent, 226 g of RPKC powder was measured into two clay-pot crucibles and subjected to pyrolysis in a muffle furnace (Gallenkamp model) at 500 °C for 15 minutes in a nitrogen environment; the resultant char was filtered *via* a 106 µm mesh and stored in airtight plastic containers until required, and this material was labelled Pyrolysed Palm-kernel Chaff (PPKC). After that, the chemical activation was carried out. 44 g of PPKC was mixed with 200 mL of 1.0 M H_3PO_4 and refluxed at 80 ºC for 4 h, then undisturbed equilibration was carried out for 20 h. The solid obtained after acid treatment was washed several times with double distilled water until the effluents were neutral and dried in an oven at 105 ºC for 48 h and sieved through 106 µm mesh, mainly according to the activation procedure reported by Barakat *et al.,* 2024; Wipawee and Attso, 2023; and Gimba *et al.,* 2001. The obtained adsorbent was stored in an airtight container until use and was labelled Chemically-Pyrolysed Palm-kernel Chaff (CPPKC).

The surface functional groups were analysed by ATR-FTIR spectroscopy (TENSOR 27, Bruker) in the range of 4000 –500 cm^{-1} at a resolution of 8.0 cm^{-1}, using 200 scans at a scan rate of 40 kHz, in accordance with the FTIR methodology previously applied to the analogous Cd^{2+} biochar system (Esho *et al.,* 2026). Surface morphology and elemental composition were further analysed by scanning electron microscopy coupled with energy dispersive X-ray spectroscopy (SEM–EDX; Hitachi SU 3500, Tokyo, Japan). Imaging and elemental mapping were performed at 30 kV and 12 keV, respectively and micrographs were taken at 500X magnification. The textural properties were determined by N_2 adsorption-desorption isotherms (ASAP2023 V4.02H, Micromeritics, USA) after degassing the samples at 437 K for 3 h. The BET surface area and the pore parameters of each adsorbent were calculated from the isotherms.

The thermal decomposition characteristics were monitored using thermogravimetric analysis (TGA; PerkinElmer Thermal Analyzer): a 5 mg dried sample, contained in a platinum crucible, was subjected to heating from 100 to 1000 ºC at a rate of 10 ºC/min under a nitrogen flow of 50 mL/min, with the weight-loss data recorded continuously as a function of temperature.

The mineralogical and crystalline-phase composition was determined by x-ray diffraction on a Shimadzu XDS 2400H diffractometer with a Cu Kα source (wavelength 1.5418 Å) at 40 kV and 30 mA. Before scanning, samples were dried in an oven at 105 ºC, ground into a fine powder, sieved to 63 micrometers, and compacted onto an acrylic holder to create a flat surface using approximately 2 g of material. Diffractograms were obtained within a 15º – 70º of 2θ range with a step increment of 0.02º and a counting duration of 2 seconds per step, and phases were identified *via* search-match analysis against the ICDD Powder Diffraction File database.

Surface-charge characteristics were evaluated through zeta potential measurements acquired using a Surpass 2 electrokinetic analyzer (Anton Paar, Graz, Austria). Suspensions of each adsorbent (approximately 8 mg) at 0.02% (w/v) in 40 mL aliquots of buffer at pH 2, 4, 6, 7, 8, 10 and 12 were prepared; they were well stirred and allowed to stand for 5 minutes before the supernatant was drawn into the capillary cell of the analyser. Electrophoretic mobility measurements were performed in triplicate, during a 30 s injection for each assessment and converted into zeta potential using the Smoluchowski equation.

2.3 Batch Adsorption Studies, Modeling and Statistical Analysis

Batch experiments were conducted by mixing a specified mass (e.g., 0.05 g) of each synthesised adsorbent (RPKC, PPKC, CPPKC) with 20 mL of lead(II) solution in 50 mL sample containers, stirred at 150 rpm on an electric thermostatic shaker. The lead(II) working solutions were prepared by serial dilutions from a stock solution of 1000 mg/L prepared by dissolving 1.60 g of $Pb(NO_3)_2$ in 1 L of distilled water. Series of experiments were performed to investigate the effect of solution pH (2, 4, 6, 8 and 10, adjusted with 0.5 M HCl and 0.5 M NaOH), contact time (2, 5, 10, 15, 20, 30, 60, 240 and 480 min), initial concentration (50, 100, 150, 200, 300, 400, 500, 600 and 800 mg/L), adsorbent dose (0.01, 0.02, 0.04, 0.06, 0.08 and 1.0 g) and temperature (25, 40, 50 and 60 °C) on lead(II) uptake. The spent adsorbent was separated after equilibrium by filtration for each run and the residual lead(II) concentration in the solution was determined by atomic absorption spectrophotometry (AAS; Perkin Elmer Analyst 700 model). Aliquots of the working solutions before the adsorption process were also analysed to confirm the exact initial lead(II) concentrations. All the experiments were performed in triplicate and the average values were taken for analysis. The percentage of adsorption and amount of lead(II) adsorbed at equilibrium (Q_e) was calculated from the obtained data using Equations 1 and 2 respectively.

$$\%Adsorption = \frac{C_o - C_e}{C_o} \cdot 100 \qquad 1$$

$$Q_e = \frac{(C_o - C_e)V}{m} \qquad 2$$

C_o is the initial concentration of lead(II) in milligrams per liter (mg/L), C_e is the equilibrium concentration of lead(II) in milligrams per liter (mg/L), V is the volume of the lead(II) solution used in the experiment (L) and m is the mass of the adsorbent in grams (g).

The temporal adsorption data were analyzed using three non-linear kinetic models: pseudo-first order, pseudo-second order, and Avrami fractional, as delineated in **Equations 3 – 5**, respectively. The kinetic data underwent analysis *via* the intraparticle diffusion model (**Equations 6**), while the concentration and temperature-dependent (isothermal) data were

further examined utilising non-linear representations of the Langmuir, Freundlich, and Liu models, as delineated in **Equations 7 – 9**.

$$Q_t = Q_e\left\{1-\exp(-k_f t)\right\} \quad 3$$

$$Q_t = \frac{Q_e^2 k_s t}{k_s Q_e t + 1} \quad 4$$

$$Q_t = Q_e\left\{1-\exp(-k_{Av} t)^{n_{Av}}\right\} \quad 5$$

$$Q_t = k_{id} t^{0.5} + C \quad 6$$

$$Q_e = \frac{Q_{\max} K_L C_e}{1+(K_L C_e)} \quad 7$$

$$Q_e = K_F C_e^{\frac{1}{n_F}} \quad 8$$

$$Q_e = \frac{q_{\max}(K_g \cdot C_e)^{n_g}}{1+(K_g \cdot C_e)^{n_g}} \quad 9$$

In the expressions above, the quantity (mg) of the adsorbate (Pb^{2+}) retained (Q_t) by 1 g of the adsorbents at a specified time, t; k_f (min^{-1}) indicates the pseudo-first-order rate constant; k_s (g mg^{-1} min^{-1}) pertains to the pseudo-second-order rate constant; k_{AV} represents the rate constant of the Avrami fractional-order model (min^{-1}); n_{AV} denotes the Avrami exponent, associated with the fundamental adsorption mechanism; k_{id} refers to the intraparticle diffusion rate constant (mg g^{-1} $min^{-0.5}$); C (mg g^{-1}) pertains to the boundary layer thickness as the intraparticle diffusion constant; Q_{max} indicates the maximum adsorption capacity of the adsorbent (mg g^{-1}); C_e is the equilibrium concentration of the chaff adsorbent (mg L^{-1}); K_L is the Langmuir equilibrium constant (L mg^{-1}); K_F is the Freundlich equilibrium constant $\left((mg\ g^{-1})(mg\ L^{-1})^{-\frac{1}{n_F}}\right)$; n_F is the Freundlich exponent; K_g is the rate constant of the Liu model (L mg^{-1}); and n_g represents the adsorption intensity (dimensionless).

Thermodynamic formulas (**Equations 10 and 11**) were employed to determine the standard change in Gibb's free energy ($\Delta G°$, kJ mol^{-1}), standard change in enthalpy ($\Delta H°$, kJ mol^{-1}), and standard change in entropy ($\Delta S°$, J mol^{-1}K^{-1}).

$$\Delta G^o = -RT\ln K \qquad 10$$

$$\ln K = \frac{\Delta S^o}{R} - \frac{\Delta H^o}{RT} \qquad 11$$

where R is the universal gas constant (8.314 J mol-1 K-1) and T is the temperature in Kelvin (K). Non-linear curve fitting and parameter calculations were executed using OriginPro. The metrics of the adjusted coefficient of determination (R^2_{adj}) and the reduced chi-square (χ^2_{red}) for each model were utilised to identify the optimal model for the adsorption data. The statistical representations of R^2_{adj} and χ^2_{red} are delineated in **Equations 12 and 13**, respectively.

$$R^2_{adj} = \left\{1-(1-R^2)\right\}\left\{\frac{n-1}{n-p-1}\right\} \qquad 12$$

$$\chi^2_{red} = \left\{\frac{1}{n-p}\right\}\sum_i^n \left(q_{i,\exp} - q_{i,\mathrm{mod}el}\right)^2 \qquad 13$$

where n denotes the quantity of data points; p represents the count of parameters within the model, while $q_{i,model}$ and $q_{i,exp}$ signify the specific data point forecasted by the model and acquired *via* experimentation, respectively. A value approaching one indicates a good fit of the curve by the model (Aiyesanmi et al., 2022).

3. Results and Discussion

Adsorbents (RPKC, PPKC and CPPKC) were synthesised from PKC and characterised. The three adsorbents were tested for the uptake of lead(II) from simulated water by batch adsorption method.

3.1 Characteristics of the Adsorbents

The Fourier Transform Infrared spectra of RPKC, PPKC and CPPKC (**Figure 1**) have shown significant differences in functional groups indicating the effect of pyrolysis and chemical

activation on palm kernel chaff. The interaction of the adsorbents with Pb^{2+} can be explained well by the different functional groups present in the adsorbents. The peak at 3386 cm^{-1} in RPKC is assigned to the −OH group, 2960 cm^{-1} is assigned to the C–H stretch of an alkane moiety, 1614 cm^{-1} corresponds to the aromatic C=C stretching vibration, 1442 cm^{-1} is assigned to the C–H bending vibration in aromatics, 1219 cm^{-1} is assigned to the C–O stretching vibration and the 794 cm^{-1} peak is assigned to the out-of-plane bending vibration of aromatic C-H. PPKC shows absorption peaks at 2664 cm^{-1}, 2221 cm^{-1}, 1718 cm^{-1}, 1426 cm^{-1} and 601 cm^{-1}, which are associated with distinct C–H, C≡N or C≡C, carbonyl functionalities, aromatic C=C or aliphatic C–H bending, and inorganic mineral remnants or deformations of aromatic rings, respectively.

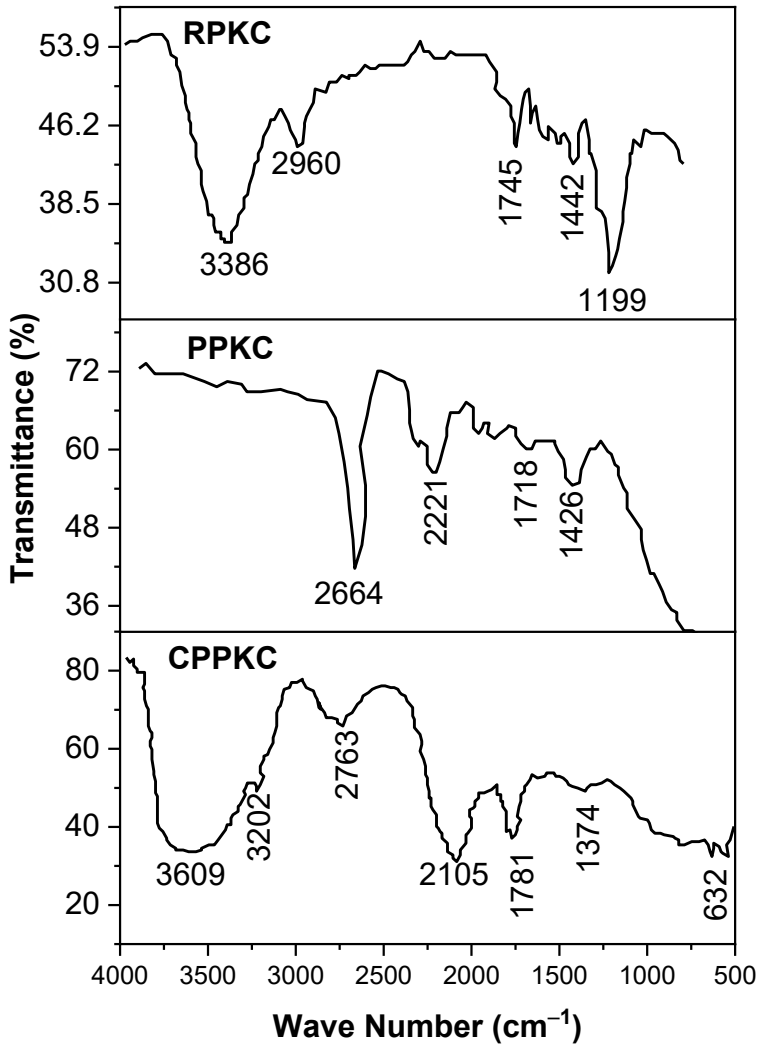


Figure 1: FTIR spectra of the RPKC, PPKC and CPPKC

PPKC described the chemical reactions of functional groups during pyrolysis, (e.g., O-H elimination and C≡N insertion) by Liu et al., 2023. O-H (free and hydrogen bonded), C-H (aliphatic or aldehyde) stretching, C≡N or C≡C, stretching of carbonyl, C-H bending and vibrations of aromatic or inorganic compounds. The broad bands at 3609 and 3202 cm^{-1}, 2763 cm^{-1}, 2105 cm^{-1}, 1781 cm^{-1}, 1374 cm^{-1} and 632 cm^{-1} in CPPKC. The hydrophilic nature was confirmed by the detection of O–H and aliphatic groups (Raj et al., 2025)

The higher adsorption is attributed to the surface complexation of the adsorbent due to oxygen functional groups including O-H, C=O and C-O. The aromatic and aliphatic parts can increase the π-π and hydrophobic interactions with pollutants (Danso-Boateng *et al.,* 2021; Qing *et al.*, 2024; Yang *et al.,* 2025).

The TGA of RPKC (**Figure 2**) shows a decrease of moisture content (25.86%) from 200 to 450 ℃. The weight loss of 62.48% is attributed to the fracture of hemicellulose and cellulose in the range of 450-600 ℃. Lignin decomposed with a loss of 5.44% and a residue of 5.44% at a temperature of 600 − 800°C. Palm kernel biomass decomposes to large amounts of volatiles (Ewa *et al.,* 2024). High Content of Cellulose. Likewise, raw palm-kernel biomass is heated to obtain low carbon mass (Dechapanya and Khamwichit, 2023).

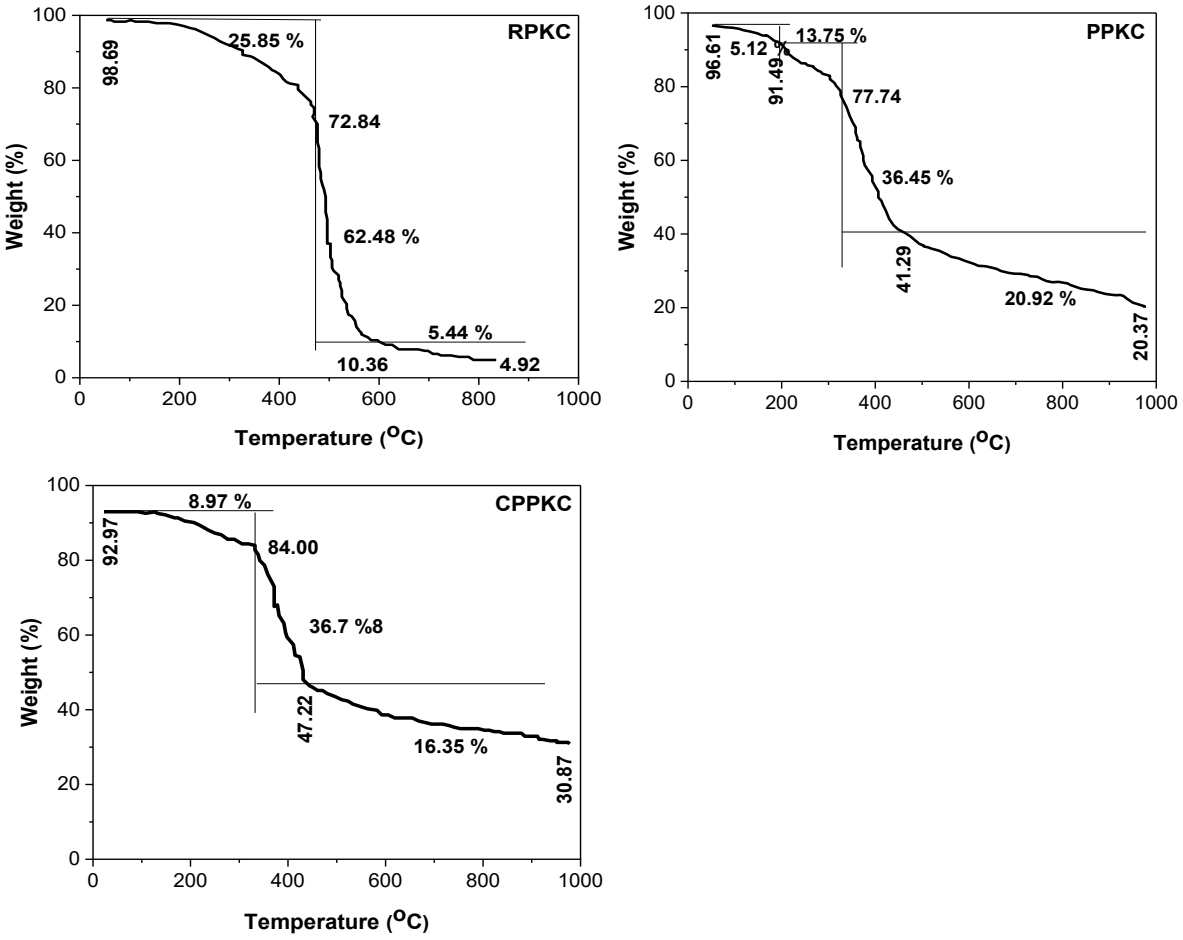


Figure 2: TGA profiles of RPKC, PPKC and CPPKC

In PPKC, 5.12 % moisture is removed in the temperature range 50–200 °C and 50.2 % cellulosic substances are degraded in the temperature range 200 – 450 °C, with 20.37 % residue at 950 °C. This leads to the degradation of cellulose, hemicellulose and lignin components (Tiwari *et al.,* 2024).

In CPPKC, the weight loss was considerable between 100 ℃ and 300 ℃, which was 8.97% and between 300 ℃ and 400 ℃, the loss was 36.78%. In the temperature range of 400 - 950 ℃, it was 16.36 % lower, with a carbon residue of 30.97 %. The thermal improvement contributes to the good stability of CPPKC due to the formation of polyphosphate and phosphate-ester chains which are stable at high temperatures, thus preventing decomposition under high temperature conditions and the adsorbent degrades early (Zhu *et al.,* 2024). The thermal stability of the adsorbents was found to be in the order of RPKC (5.44%) < PPKC (20.37%) < CPPKC (30.97%). This study demonstrated the effects of physical and chemical changes on the thermal properties. RPKC failed quickly and was less stable. The first pyrolysis resulted in

better stability and char yield for PPKC. The CPPKC suggested that the combination of catalytic decomposition and structural stabilization improved char retention.

The SEM micrographs of the adsorbents are shown in **Figure 3.** Morphological insights of the adsorbents obtained from biomass materials at different treatment stages. The surface structures obtained by RPKC correspond to a dense and chaotic fibrous arrangement related to biomass rich in lignin and cellulose and with low porosity. The low porosity of palm-kernel shells and coconut husks, due to their small size and chaotic configurations, reduced the adsorption ability (Hadi *et al.,* 2024).

PPKC has broken and fragmented fibrous structures with the increase of the number of microscopic holes and cracks due to pyrolysis. This is due to the degradation of cellulose and hemicellulose creating larger voids *via* de-volatilisation. Which in turn increased the porosity of the adsorbents (Benregga *et al.,* 2021). The decrease of lignin and hemicellulose content without the decrease of cellulose level will be beneficial for the increase of surface area and pore volume (Xing *et al.,* 2023).

The CPPKC has greater porosity, more cavities and channels after pyrolysis and chemical activation with H_3PO_4 than the other two adsorbents. The use of H_3PO_4 determines the connection of lignin and cellulose, which also reveals the sponge-like structure, increasing the surface area and pore volume that enhances the adsorption capacity for wastewater (Liang *et al.,* 2023; Kumari *et al.,* 2024).

The EDX spectra in **Figure 4** illustrate the surface elemental composition and variability. The adsorbent RPKC consists of 46.39% carbon, 39.26% oxygen, 5.86% magnesium, 2.10 % silicon and 1.33% calcium. The polar functional groups in the adsorbent facilitate complexation and ion exchange process. It is high in oxygen that improves the adsorption (Mahmoud *et al.,* 2024). Other mineral elements such as calcium and magnesium facilitate the adsorption in aqueous solution by means of ion exchange mechanisms. (Almanassra *et al.,* 2021; Samaraweera *et al.,* 2023)

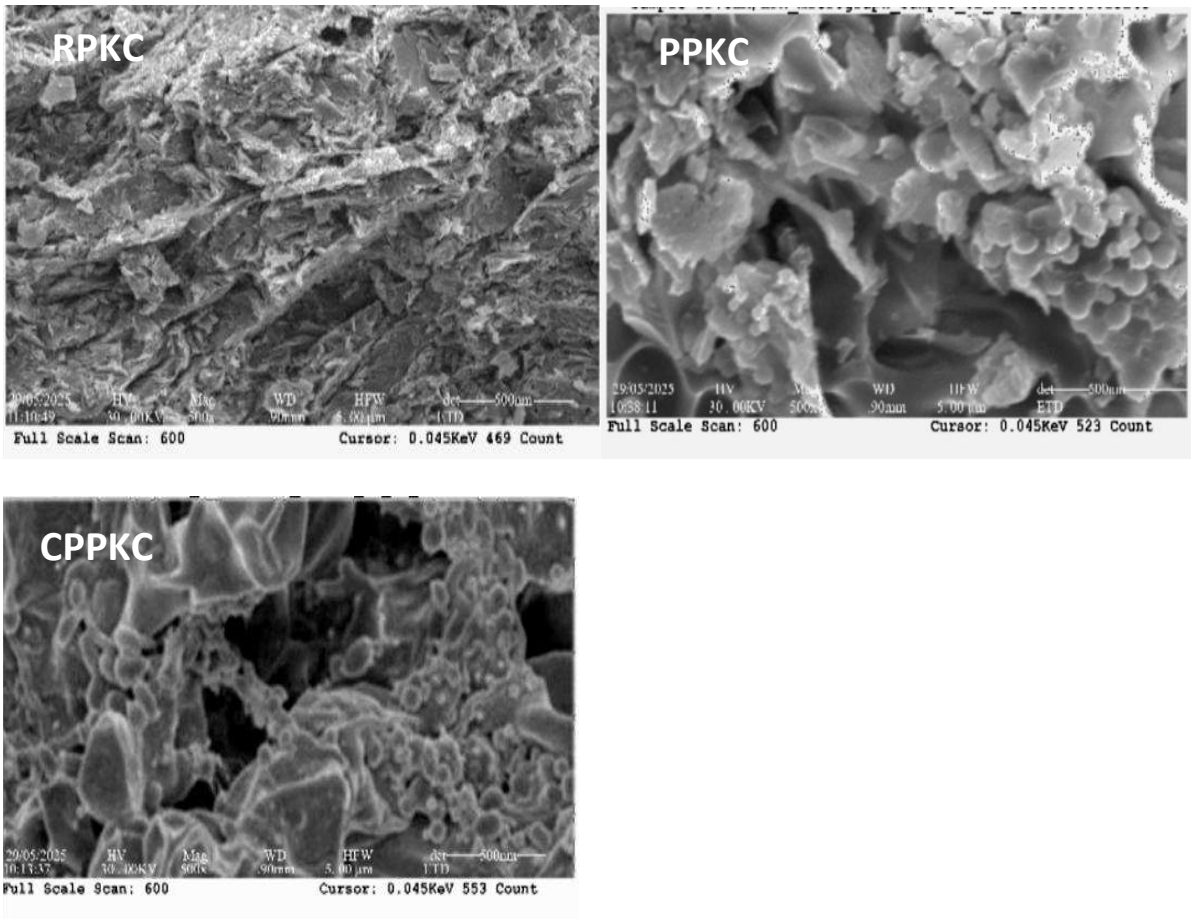
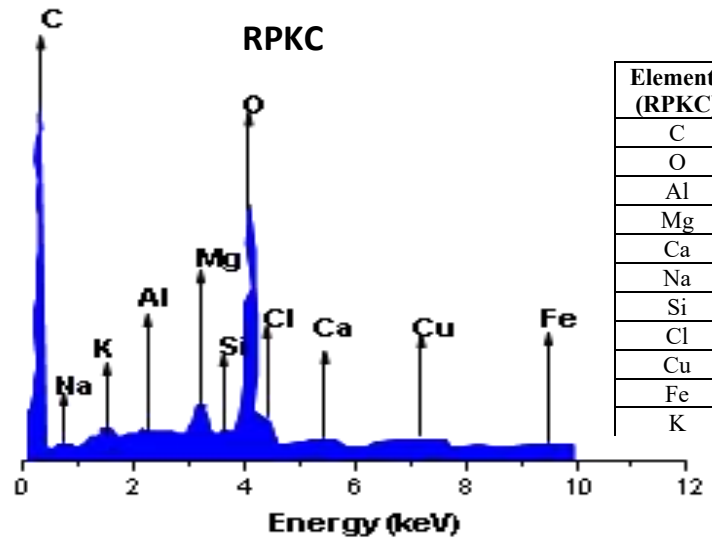
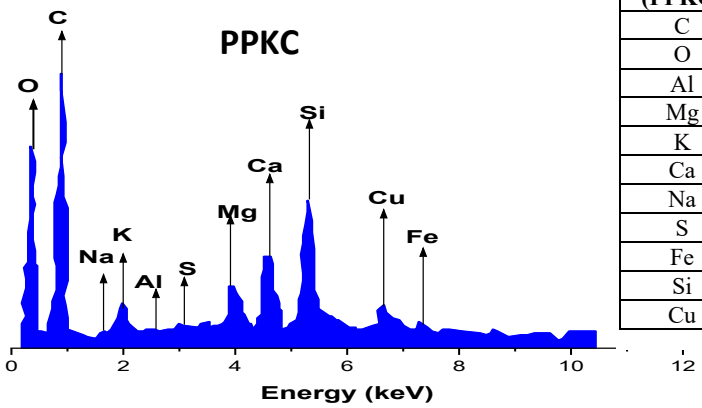


Figure 3: Scanning electron micrographs of RPKC, PPKC and CPPKC

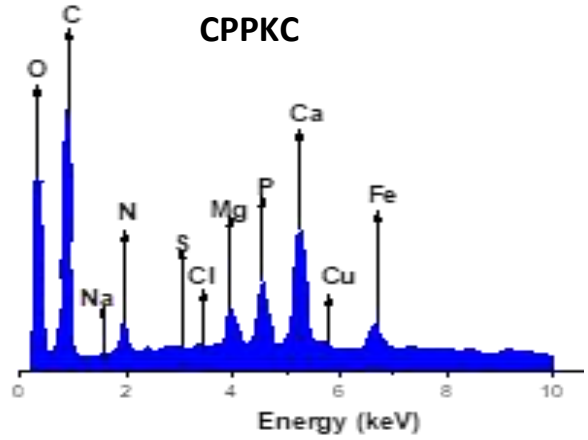
The PPKC contained 52.34 % C and RPKC contained 7.46% Ca and 9.32% Si. The silicate enriched biochar had a good surface area leading to a better adsorption of heavy metals thru mechanisms like ion exchange, surface precipitation and complexation (Tong *et al.,* 2021). Some mineral components (i.e., Ca, Mg, and Si) can be plant nutrients and increase adsorption capacity (Shi *et al.,* 2023). Trace amounts of iron, copper and aluminum can contribute to the formation of free radicals which improve the redox process and the formation of more active adsorption pores However, spectroscopic signals can be hindered by copper and iron (Xie *et al.,* 2024).



Elements (RPKC)	Percentage (%)
C	46.39
O	39.26
Al	0.95
Mg	5.68
Ca	1.33
Na	1.67
Si	2.10
Cl	0.54
Cu	0.21
Fe	0.32
K	1.27



Elements (PPKC)	Percentage (%)
C	52.34
O	24.41
Al	1.20
Mg	0.93
K	1.10
Ca	7.46
Na	0.52
S	0.86
Fe	0.73
Si	9.32
Cu	1.00



Elements (CPPKC)	Percentage (%)
C	57.91
O	28.98
Cl	1.14
Mg	1.30
P	1.75
Ca	5.07
Na	0.41
S	0.52
Fe	0.15
N	2.48
Cu	0.20

Figure 4: EDX spectra of RPKC, PPKC and CPPKC

EDX spectrum of CPPKC showed 57.91% carbon, 28.98% oxygen, 1.75% phosphorus and 2.48% nitrogen. The increase in the number of active sites (Liu et al., 2024) was attributed to the co-doping of nitrogen and phosphorus in the carbon matrix with more functional groups. The results are attributed to interactions of π–π electron donors and acceptors, redox reactions and electrochemical conductivity. In addition, the polarity and reactivity of the nitrogen and phosphorus treated adsorbent surface were higher, which increased the energy storage capacity and ecological relevance of the adsorbent (Cheng *et al.,* 2022).

The zeta potential (**Figure 5**) is an important parameter to evaluate the surface charge properties of adsorbents and, therefore, their interaction behaviors with ionic contaminants in water. The pH where the net surface charge of the adsorbent becomes zero is called the point of zero charge (*PZC*) and it controls whether the adsorbate–surface interaction will be dominated by protonation or deprotonation of surface sites. The results showed that the point of zero charge (*PZC*) values of RPKC, PPKC and CPPKC are 5.53, 5.39 and 5.19, respectively in the pH range of 2 - 12. When the pH of the solutions of adsorbents decreases below the point of zero charge, the surfaces of adsorbents have a notably positive charge, which increases the absorption of anions. When the solution pH exceeds the respective point of zero charge, the adsorption of cations intensifies. The raw palm-kernel chaff (RPKC) attains the maximum value of point of zero charge (*PZC*) indicating a lesser presence of specific acidic functional groups such as phenolic, lactonic and carboxyl groups which can easily break the electrical charge balance at the surfaces of the adsorbent (Sobik-Szołtysek *et al.,* 2021). The presence of functional groups such as carboxylic esters, ether-alcohols and aliphatic groups has increased the negative charge on the microplastic particle surfaces at a solution pH above 2.0 thus continuously amplifying the density of acid sites (Jui-Yen *et al.,* 2023). The lower *PZC* values observed for PPKC and CPPKC could be due to the presence of mineral oxides, phosphorus, and nitrogen in the adsorbents. These heteroatoms can readily influence the electron distributions and thus change the surface charge properties by increasing the surface acidity and then decreasing the *PZC* (Pan *et al.,* 2022).

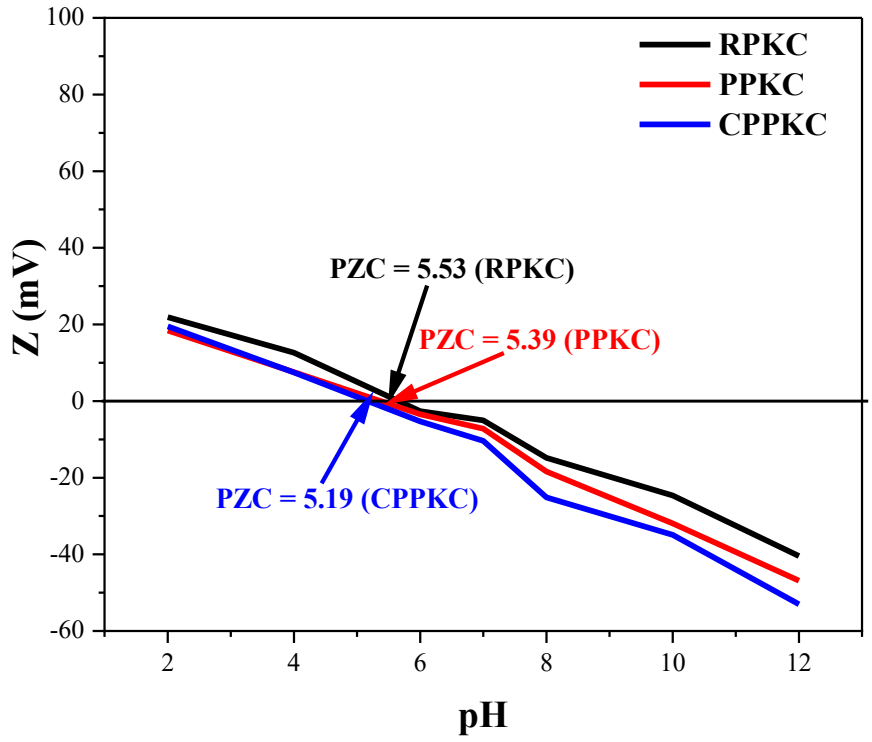


Figure 5: Zeta potentials of RPKC, PPKC and CPPKC

Figure 6 shows XRD spectra of the adsorbents. RPKC exhibits peaks at 16° (010), 20° (200) and 34° (112). In PPKC, the application of heat to the samples leads to structural disintegration and changes of the mineral components. The disruption of the networks formed by crystalline cellulose and the formation of new mineral structures are observed as well as a decrease of the intensity of peaks at planes 010 and 200. The adsorbent CPPKC shows the transformation of structures into a more disordered system due to the creation of highly porous amorphous networks, resulting in increased surface areas, which enhance the adsorption process. The crystalline cellulose is shown to be present in the RPKC in the 010 and 200 planes (Khandoker *et al.,* 2023). The sharpness of the peaks and their organized arrangement represent RPKC in its native form (Chakraborty *et al.,* 2022). The structure of plane 110 was lignocellulosic, a feature which is associated to amorphous carbon (Hadi *et al.,* 2024). The research work performed in the recent years on the agricultural by-products has shown the presence of various properties in them which resulted in crystalline minerals such as calcite (25°, 104 plane), aromatic lignin (33.4°, 112 plane) and potassium oxide (39.2°, 202 plane). The thermal energy increase in PPKC causes more changes in the structural networks (Bondar, 2022). Minerals are recorded such as potassium oxide (28.2°), sylvite (40°), and magnetite (43.2°) (Wang *et al.,* 2022). The complete formation of a non-crystalline network in the physically and chemically pyrolyzed sample (CPPKC) causes the removal of mineral components and the

restructuring of lattice frameworks, which facilitates the increase of high surface areas and enhances the porosity of the biochar. This corresponds to the increase in adsorption capacity of biochar for the remediation of environments polluted with inorganic and organic pollutants (Song *et al.,* 2024).

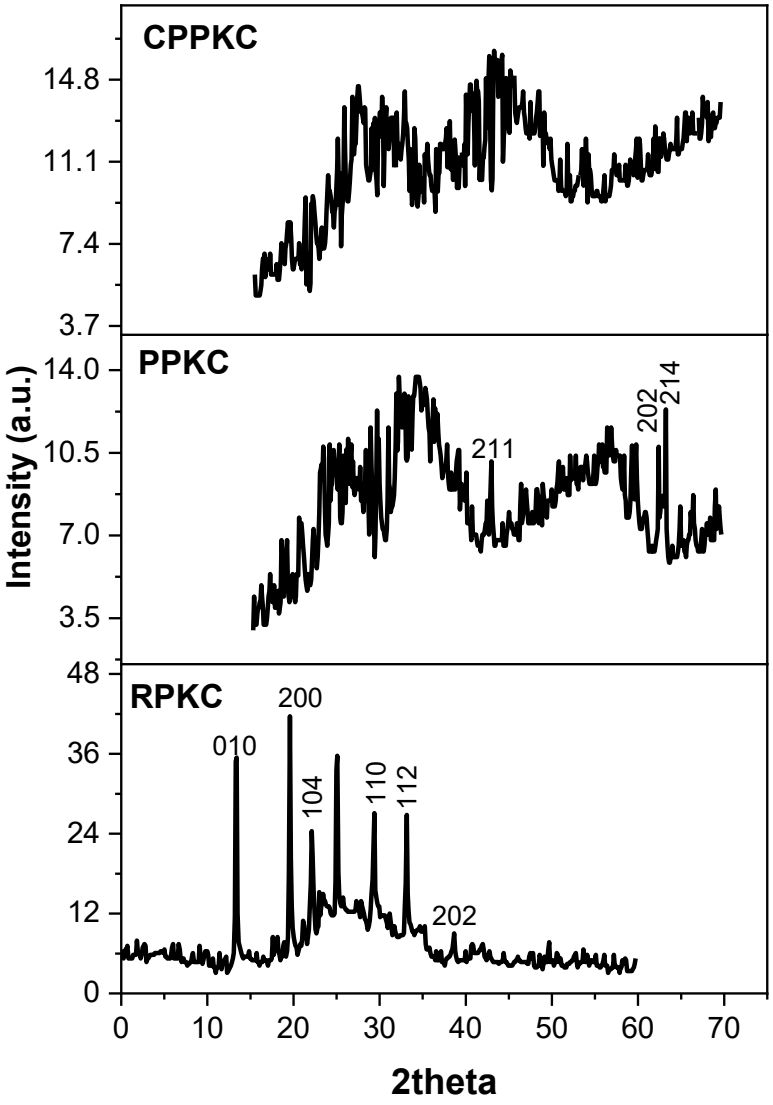


Figure 6: X-ray diffraction (XRD) of the adsorbents

Table 1 presents the nitrogen adsorption-desorption characteristics of the adsorbents. The BET surface area of RPKC is 109.095 m^2 /g with pore diameter of 2.1497 nm and pore volume of 0.4931 cm 3 /g. The BET surface area of PPKC is 114.638 m^2/g, the pore diameter is 2.3004 nm, and the pore volume is 0.6210 cm^3/g. The BET surface area of CPPKC is 116.132 m^2/g, with the pore diameter of 2.3752 nm and

the pore volume of 1.4327 cm^3/g. As pointed out by Neme *et al.,* 2022; Zakaria *et al.,* 2023, the pore accessibility for penetration and adsorption of pollutants was increased with the slow increase of PPKC and CPPKC in the surface areas with temperature from 400 - 600 ℃. The pore volume of PPKC and CPPKC increases dramatically from 0.6210 to 1.4327 cm^3/g. This is due to the activation with H_3PO_4 during the pyrolysis process. It will increase the formation of more pores for adsorption. Moreover, it will enhance the cross-linking, dehydration, and formation of thermally stable phosphate esters to avoid the pore collapse (Dechapanya and Khamwichit, 2023; Neme et al., 2022).

The pore sizes (2.15-2.38 nm) of the adsorbents studied in this work belong to the mesopores. Mesoporous adsorbents effectively adsorb Pb^{2+} from aqueous solutions due to their efficient intra-particle diffusion of adsorbates. The increased pore volume resulted in the pore expansion and fusion. The combination of micro-pores to meso-pores leads to a significant increase of the total pore volume, but the specific surface area does not increase proportionally, and may even decrease in some cases (Neme *et al.,* 2022). The partial plugging of the pores by the incomplete removal of phosphate residues may hinder passage of nitrogen gas during the process. However, the blocked sites of the aqueous adsorption systems can show chemical reactivity and improve the metal uptake *via* ion exchange, precipitation, or complexation (Dechapanya and Khamwichit, 2023). The integrated physical and chemical activation (CPPKC) generally produced the best trade-off of surface area, pore size and pore capacity. Beside the texture improvement, the treatment with H_3PO_4 is known to introduce functional groups derived from phosphorus that could increase the affinity for metal cations through complexing and precipitation mechanisms. Thus, a higher elimination efficiency of CPPKC toward Pb^{2+} than that of RPKC and PPKC is expected.

Table 1: BET data of RPKC, PPKC and CPPKC

Adsorbent	BET Surface area (m^2/g)	Pore diameter (nm)	Pore volume (cm^3/g)
RPKC	109.09	2.1497	0.49310
PPKC	114.64	2.3004	0.62100
CPPKC	116.13	2.3752	1.4327

3.2 Adsorption Performances of RPKC, PPKC and CPPKC at varying pH Values

The initial pH of the solution is a key parameter in adsorption studies because it influences the overall surface charge of the adsorbent and the speciation of the adsorbate in the solution. The initial pH of the solution in the adsorption studies affects the electrostatic interactions between the adsorbent and the

adsorbate, and thus, the adsorption efficacy of the adsorbents and the adsorption mechanisms involved (e.g., physical adsorption, ion exchange, etc.). **Figure 7A** shows that the adsorption maximum of lead (II) ions is recorded at pH = 6.0 for all the three adsorbents. This observation may be related to the surface charge of the adsorbents, which is shown by the P_{ZC} data, where the deprotonation of functional groups caused an increased surface negative charge that facilitates complexation with Pb^{2+} when pH values are above P_{ZC}. At pH 6.0, the surface of CPPKC carries more negative charges, resulting in more adsorption of cations. The adsorption of the adsorbate by the adsorbents increased with increase of pH from 1 to pH 6 and then decreased as pH increase to 6.0. Adsorption increases gradually from pH 1 to 5, which may be due to the competitive interaction between H^+ and Pb^{2+} ions. At pH 6.0, complexation and electrostatic interactions at the surfaces are optimized. The adsorption was decreased as the pH value increased over 6.0 due to hydroxides precipitation. In the present study, the highest adsorption capacity for the removal of lead(II) from water solutions was observed for CPPKC. as noted by Da-Silva *et al.,* 2025; Kumari *et al.,* 2021, the pH values were different and the adsorbents had more stable with more active sites and functional groups.

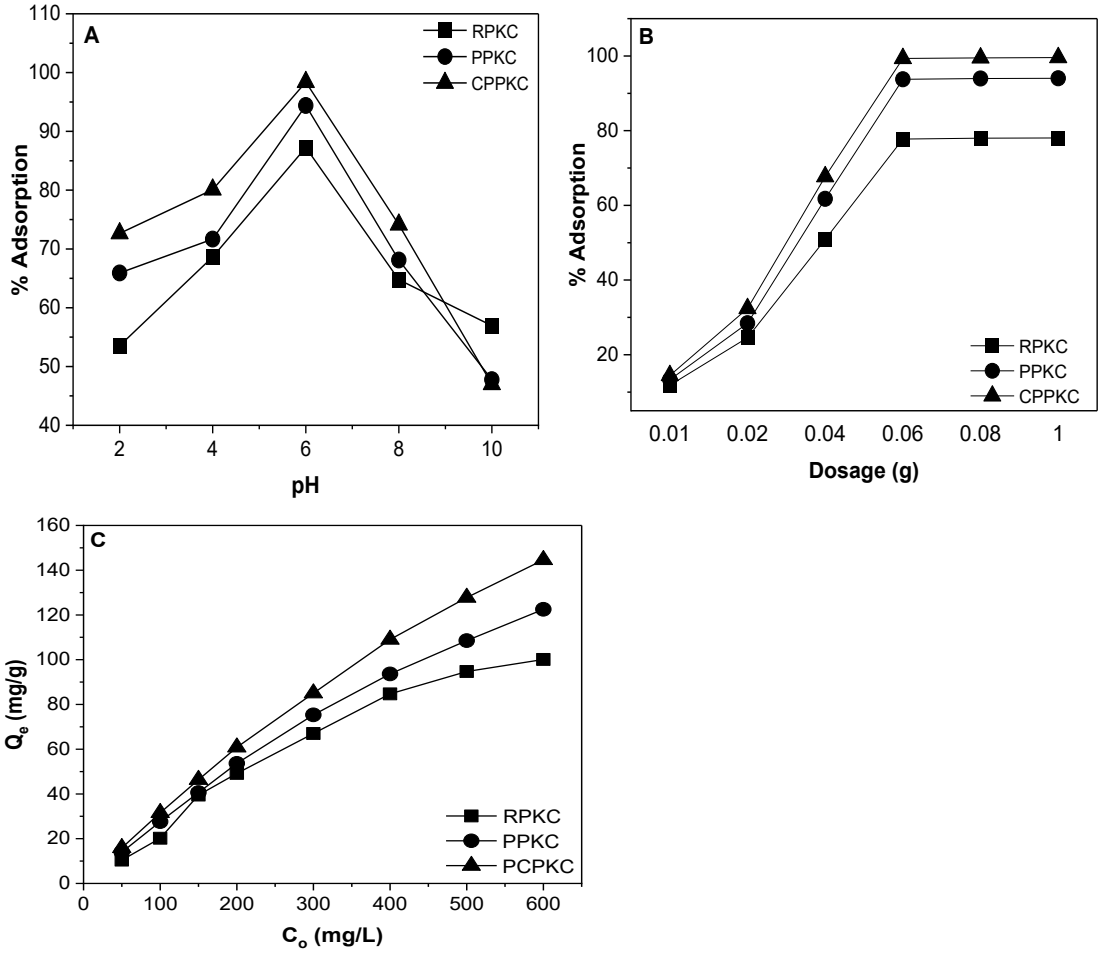


Figure 7: (**A**) pH profiles, (**B**)dosage profiles, and (**C**) effect of initial [Pb^{2+}] on adsorption of Pb^{2+} onto RPKC, PPKC and CPPKC

The effect of the adsorbent amount on the extraction of Pb^{2+} from water solutions is shown in **Figure 7B**. The increase in the dosage of adsorbent increased the percentage of Pb^{2+} ions adsorbed in all adsorbents, because of the availability of active sites on the surfaces of the adsorbents and the proliferation of functional groups that promote the remediation of Pb^{2+} ions. The best dosage of the three adsorbents for the removal of Pb^{2+} is 0.06 g. The rise in percentage of adsorbate removal is tied to the increase in adsorbent dose until a critical limit. This is attributed to the increase in adsorbent surface area and consequently, increase in active sites for adsorbate adsorption (Lima *et al.,* 2015). It can be observed from the graph that the plateau is formed at higher dosages, which is probably due to the occupation of active sites by the adsorbate molecules, thereby establishing equilibrium (El-Dein *et al.,* 2025) and any increase in the dosage of adsorbent beyond the optimum dosage will not result in a higher percentage of adsorption. Maximum adsorption efficiency is noticed in CPPKC followed by PPKC and minimum adsorption percentage is observed in RPKC. These results suggest that chemical modification greatly improved surface reactivity and binding affinity. Surface pyrolysis and chemical modification of adsorbents improve the remediation of toxic metals by having more functional groups and extra pores for adsorption (Zhang *et al.,* 2025).

Figure 7C shows the relationship between initial concentration (Co) of Pb^{2+} ions in solutions and the equilibrium adsorption capacity (Q_e) of the adsorbents analysed. The illustration shows that the equilibrium adsorption capacity (Q_e) increases with the increase of the initial concentration of lead(II) ions in all cases. The phenomenon shows that more Pb^{2+} ions are being adsorbed per unit mass of adsorbent and probably this is due to the presence of active sites on the surface of adsorbent. When the concentration increases the reaction rate and thus the driving force of mass transfer increases, which decreases the thickness of the boundary layer and increases the frequency of Pb^{2+} ions to meet and occupy the available surface binding sites. Increasing the initial heavy metal solution concentration (C_o) and equilibrium adsorption capacity (Q_e) promote ion diffusion and site utilization until all the surface sites are fully occupied (Yan *et al.,* 2023). The adsorption capacity is not affected as shown in the graph plateau at the initial concentration of 600 mg/L indicating the saturation of the active sites available. This plateau indicates that the adsorption is not taking place anymore with the addition of Pb^{2+} as the active sites are already occupied by the adsorbates. This phenomenon can be explained by the isotherm models such as the Langmuir isotherm, which means the total surface coverage under monolayer conditions is maximum adsorption capacity. In the case of CPPKC, the removal of Pb^{2+} ions are the most efficient. This is attributed to the special pore structure and the different active functional groups on the surface of adsorbent (Wang *et al.,* 2025). This increases the number of available binding sites, thus allowing Pb^{2+} to

form stronger complexation and electrostatic interactions. For high C_o levels, the adsorption capacity and the efficiency of the use of the adsorption sites are excellent for substances with high surface area and oxygenated functional groups. Generation of pores and functional groups is essential for the adsorption of dangerous metals (Yun *et al.,* 2022). Surface saturation of modified biochars is related to the increased surface porosity and reactivity of adsorbents, leading to the improved adsorption of Pb^{2+} ions from the adsorbate solution at the initial concentration (Jun *et al.,* 2024). The adsorption capacity (Q_e) is dependent on the initial concentration (C_o) of the adsorbate until the saturation point is reached where all available sites are occupied (as shown by the plateau on the graph) of the data in **Fig.7C**. Similarly, the surface chemistry and the structural characteristics of the adsorbent are the prerequisites for effective adsorption of Pb^{2+} ions.

3.3 Kinetic Modeling of the Adsorption Process

Figure 8 presents the kinetic data of the adsorption of Pb^{2+} ions onto RPKC, PPKC, and CPPKC. As shown the in figures for respective adsorbents, the removal of Pb^{2+} ions increased as the contact time increased until a plateau (equilibrium time) was reached. After the equilibrium was reached, the values of Q_t remain almost constant. At the beginning of the adsorption process, lead(II) ions diffused quickly from the solutions to the active sites on the surface of the adsorbent. After attainment of equilibrium, the active sites are saturated with lead(II) ions as time increased, hence, lead(II) ions slowly diffused to the saturated adsorbent's surface.

Estimation of the kinetic parameters of Pb^{2+} adsorption onto RPKC, PPKC, and CPPKC provided significant findings into the adsorption mechanisms, surface properties, and energetic requirements of these adsorbents through the use of different kinetic models such as pseudo-first order, pseudo-second order, Avrami, and intraparticle diffusion. These models were applied on the kinetic data are to obtain the rate constants, the order of adsorption process, and to predict the model that best described the experimental data. The kinetic profiles and parameters are represented in the **Figure 8** and **Table 2**, respectively.

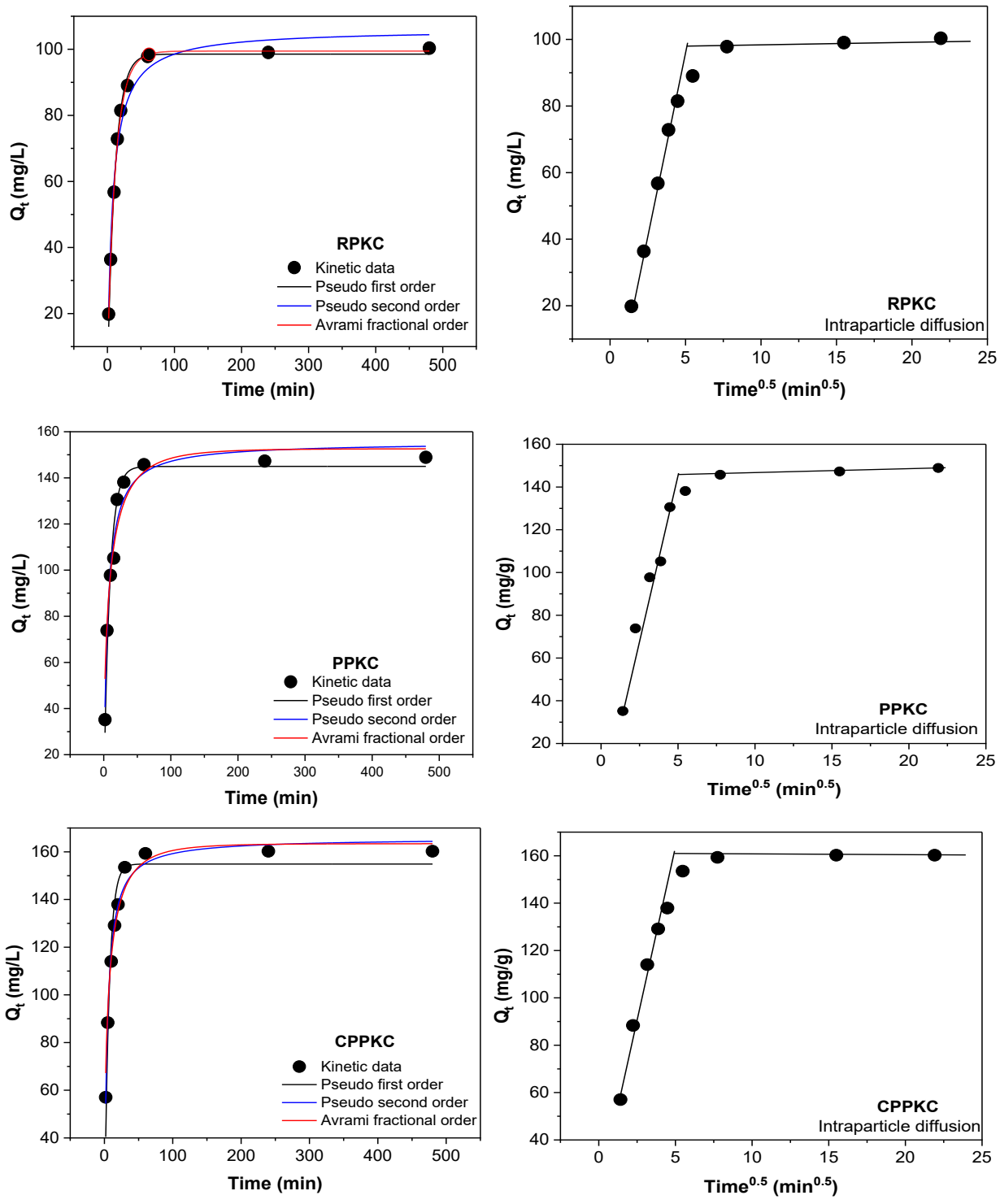


Figure 8: Kinetic profiles of RPKC, PPKC and CPPKC for adsorption of Pb^{2+}

Conditions: pH = 6; Dosage = 0.06 g; Agitation time: 2 – 480 min; Temperature= 25 ^{o}C

Table 2: Kinetic parameters for adsorption of Pb^{2+} onto RPKC, PPKC and CPPKC

Model	Parameters	Values		
		RPKC	**PPKC**	**CPPKC**
Pseudo-first order	$Q_{e,exp}$ (mg/g)	97.823	145.72	159.31
	$Q_{e,cal}$ (mg/g)	98.540	144.96	154.89
	k_f (min^{-1})	0.088610	0.11380	0.15129
	R^2_{adj}	0.99591	0.97086	0.94159
	χ^2_{red} (mg/g)	3.9710	51.422	88.510
Pseudo-second order	$Q_{e,cal}$(mg/g)	106.09	155.48	165.78
	k_s (g/mg min)	0.0012300	0.0011400	0.0014700
	R^2_{adj}	0.97930	0.97648	0.98782
	χ^2_{red} (mg/g)	20.121	41.517	18.452
Avrami fractional order	$Q_{e,cal}$ (mg/g)	99.461	152.61	163.42
	k_{AV} (min^{-1})	0.086760	0.10455	0.14717
	n_{AV}	0.90188	0.54633	0.51976
	R^2_{adj}	0.99845	0.99149	0.99042
	χ^2_{red} (mg/g)	1.7620	1.4118	1.2587
Intraparticle diffusion	k_{id} (mg/g.$min^{0.5}$)	20.681	16.914	23.388
	R^2_{adj}	0.99697	0.82882	0.96335
	C (mg/g)	–9.2443	35.193	32.895

The fitness of each model was determined by using the values of R^2_{adj} and χ^2_{red}. The best fitting model is regarded as the model with the highest value of R^2_{adj} and lowest value of χ^2_{red}. The data supplied in **Table 2** show that Avrami fractional order kinetic model provided the best fit with highest R^2_{adj} and lowest χ^2_{red}. The values of k_{AV} (Avrami fractional order rate constant) are 0.086760, 0.10455 and 0.14717 min–1 for RPKC, PPKC and CPPKC, respectively; these values signified that rate of adsorption of lead(II) on CPPKC was the fastest among the three adsorbents.

3.4 Equilibrium Description of the Adsorption Process

The equilibrium adsorption behavior primarily assesses the extent of adsorbate distribution on the surfaces of the adsorbent. The Langmuir, Freundlich, and Liu equilibrium models were employed to clarify the adsorption characteristics of Pb^{2+} ions on RPKC, PPKC, and CPPKC adsorbents across varying temperatures (25 ºC – 60 °C). The isotherm graphs and parameters are displayed in **Figure 9** and **Table 3**, respectively. The Liu model was found to be the most suitable out of the three models as it provided very high values (> 0.9999) and very low values (< 0.01 in most cases) confirming its ability to incorporate the features of the Langmuir and Freundlich models. The Liu model takes into account the different energy levels of the active sites of adsorbent surface (Naifar *et al.,* 2025). The maximum Liu adsorption capacities (Q_{max}) obtained in the present investigation are 4672.9 mg/g for RPKC at 40 °C, 4886.9 mg/g for PPKC at 40 °C and 6131.7 mg/g for CPPKC at 50 °C. The adsorbent CPPKC has the highest adsorption capacity for the extraction of aqueous lead(II) ions and the significant efficacy is due to the effect of pyrolysis and chemical activation with phosphoric acid.

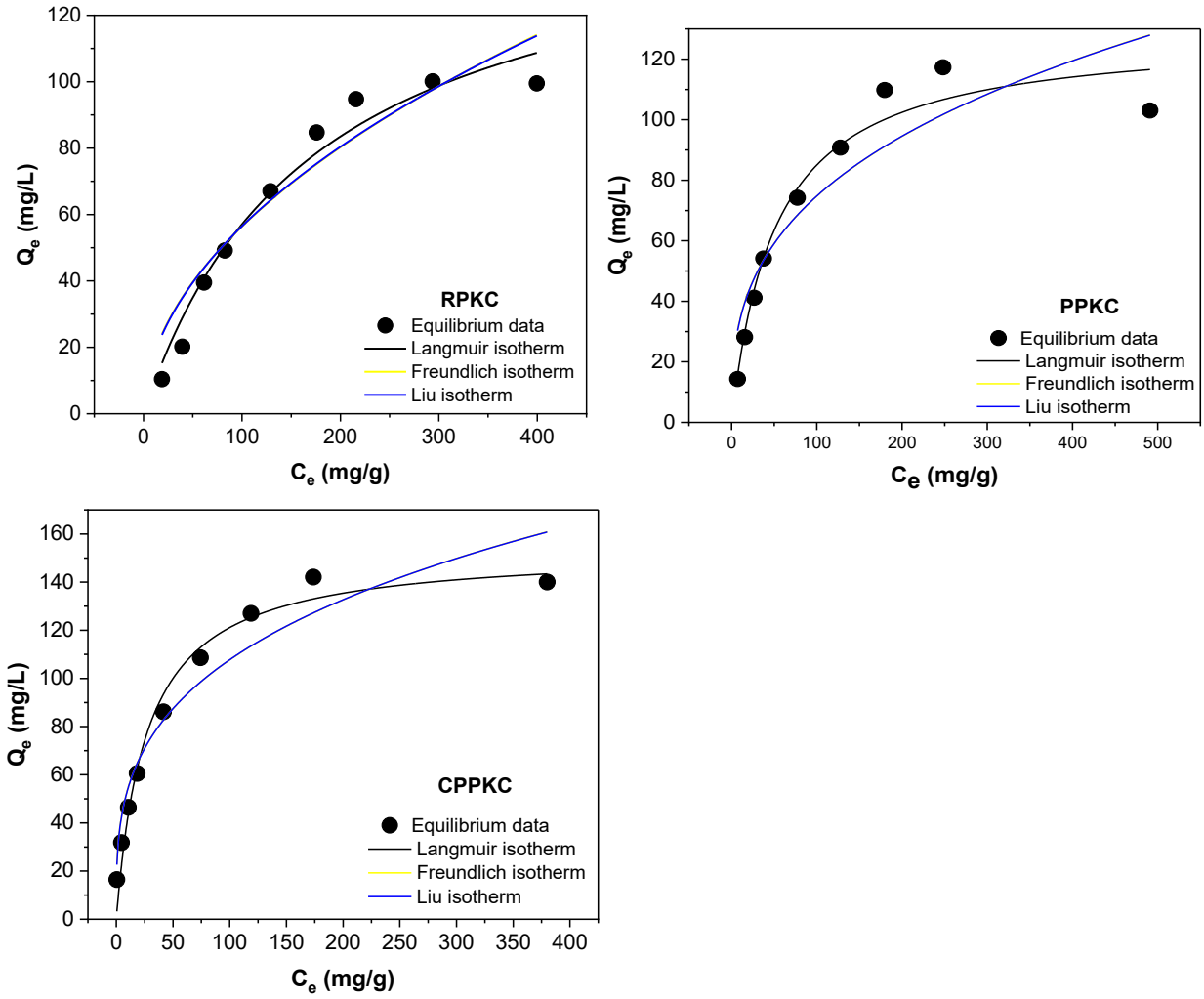


Figure 9: Equilibrium profiles for the adsorption of lead(II)

Conditions: pH = 6; dosage = 0.06 g; agitation time = 2 h; Temperature= 25°C; $[Pb^{2+}]$ = 50 – 500 mg/L

Table 3: Equilibrium parameters for adsorption of Pb^{2+} onto RPKC, PPKC and CPPKC

Model	**Parameters**	**Values**			
RPKC		**25 °C**	**40 °C**	**50 °C**	**60 °C**
Langmuir	Q_{max} (mg/g)	155.81	109.89	81.780	38.737
	K_L (L/mg)	0.0057700	0.036120	0.052779	0.092497
	R^2_{adj}	0.96426	0.94608	0.93423	0.95891
	χ^2_{red} (mg/g)	42.643	38.612	29.149	3.7652
Freundlich	$K_F\left((mg\ g^{-1})(mg\ L^{-1})^{-\frac{1}{n_F}}\right)$	5.4057	2.8784	3.0380	1.8190
	n_F	1.9641	1.8958	2.1026	2.2774
	R^2_{adj}	0.98347	0.87728	0.84971	0.88904
	χ^2_{red} (mg/g)	10.296	87.879	66.614	10.168
Liu	Q_{max} (mg/g)	1987.7	4672.9	3206.1	1335.9
	K_g (L/mg)	1.2462×10^{-5}	0.036120	0.052779	0.092497
	n_g	0.55535	0.53366	0.48226	0.44655
	R^2_{adj}	0.99999	0.99999	0.99999	0.99999
	χ^2_{red} (mg/g)	0.022390	9.3300×10^{-4}	7.1843	1.9800×10^{-4}
PPKC					
Langmuir	Q_{max}(mg/g)	128.79	133.73	94.129	79.489
	K_L (L/mg)	0.011292	0.025890	0.039412	0.059387
	R^2_{adj}	0.96346	0.91888	0.95122	0.94757
	χ^2_{red} (mg/g)	58.968	118.36	33.578	25.065
Freundlich	$K_F\left((mg\ g^{-1})(mg\ L^{-1})^{-\frac{1}{n_F}}\right)$	15.730	8.7449	6.5108	5.53784
	n_F	2.9548	2.3952	2.4859	2.5114
	R^2_{adj}	0.84173	0.80401	0.84901	0.85086
	χ^2_{red} (mg/g)	255.39	285.96	103.93	71.303
Liu	Q_{max} (mg/g)	3862.5	4886.9	3224.1	4147.7

	K_g (L/mg)	0.012027	0.025087	0.032187	0. 071151
	n_g	0.34648	0.42448	0.40968	0.40300
	R^2_{adj}	0.99999	0.99999	0.99999	0.99999
	χ^2_{red} (mg/g)	0.0051607	0.0029333	0.0015898	4.6133×10^{-4}
CPPKC					
Langmuir	Q_{max}(mg/g)	144.97	141.36	121.05	108.42
	K_L (L/mg)	0.15420	0.19134	0.21359	0.23843
	R^2_{adj}	0.96606	0.94733	0.96678	0.92126
	χ^2_{red} (mg/g)	85.450	118.69	45.476	89.063
Freundlich	$K_F\left((mg\ g^{-1})(mg\ L^{-1})^{-\frac{1}{n_F}}\right)$	30.479	26.048	14.077	13.718
	n_F	3.6555	3.5192	2.9215	3.0829
	R^2_{adj}	0.87888	0.79645	0.84591	0.77207
	χ^2_{red} (mg/g)	304.93	485.73	210.93	257.82
Liu	Q_{max} (mg/g)	2557.5	2661.1	6131.7	4977.1
	K_g (L/mg)	0.15420	0.19134	0.21359	0.23843
	n_g	0.28632	0.29603	0.34701	0.32939
	R^2_{adj}	0.99997	0.99997	0.99999	0.99999
	χ^2_{red} (mg/g)	0.024775	0.017196	0.0014938	0.0012858

3.5 Thermodynamic Characteristics of the Adsorption Process

The adsorption characteristics of the adsorbents at varying temperature levels were forecasted by assessing thermodynamic parameters. The selected temperature range in this study significantly affects the adsorption process. The thermodynamic information regarding standard enthalpy change ($\Delta H°$), standard entropy change ($\Delta S°$), standard Gibb's free energy ($\Delta G°$), and the linear van't Hoff plots of $ln\ K_g$ versus T^{-1} for the adsorbents is illustrated in **Table 4 and Figure 10**. The thermodynamic information was analysed to verify the influence of temperature on the adsorption mechanism. The standard Gibb's free energy ($\Delta G°$) values varied from 14.764 to −8.1758 kJ/mol for RPKC, from –2.1059 to −6.9491 kJ/mol for PPKC, and from –8.5476 to

−10.797 kJ/mol for CPPKC, within the temperature spectrum of 298 K to 333 K. The negative values of $\Delta G°$ validate the spontaneity (excluding RPKC at 298 K) and viability of the process.

The standard enthalpy change ($\Delta H°$) and standard entropy change ($\Delta S°$) data values were derived from the slopes and intercepts of van't Hoff's plots. The adsorption mechanism was endothermic (Ahsan *et al.,* 2018). Positive $\Delta S°$ values for the adsorbents investigated for Pb^{2+} removal suggested an increase in disorder or randomness at the solid-liquid interface. In the research, standard entropy change has been used to determine the adsorption mechanism. The values of $\Delta S° > 10$ J/mol K and $\Delta S° < 10$ J/mol K are related to the dissociative and associative mechanism, respectively (Abbasizadeh *et al.,* 2014; Shafiee *et al.,* 2020). The main mechanism of this work is dissociative since the values of $\Delta S°$ obtained are higher than 10 J/mol K for Pb^{2+} adsorption.

Table 4: Thermodynamic Parameters for Pb^{2+} for PKC

Adsorbent	**Temperature (K)**	K_g **(L/mg)**	K_g **(m^3/mol)**	ΔG^o **(kJ/mol)**	ΔS^o **(J/mol K)**	ΔH^o **(kJ/mol)**	R^2_{adj}
RPKC	298	1.2500 x 10^{-5}	2.7469	14.764	664.10	209.08	0.80643
	313	0.036120	7.4841	–5.2378			
	323	0.052779	10.936	–6.4237			
	333	0.092497	19.165	–8.1758			
PPKC	298	0.011292	2.3396	–2.1059	124.50	34.539	0.99999
	313	0.025890	5.3656	–4.3718			
	323	0.039412	8.1662	–5.6394			
	333	0.059387	12.305	–6.9491			
CPPKC	298	0.15420	31.500	–8.5476	60.519	9.3592	0.99985
	313	0.19134	39.646	–9.5764			
	323	0.21359	44.256	–10.178			
	333	0.23843	49.402	–10.797			

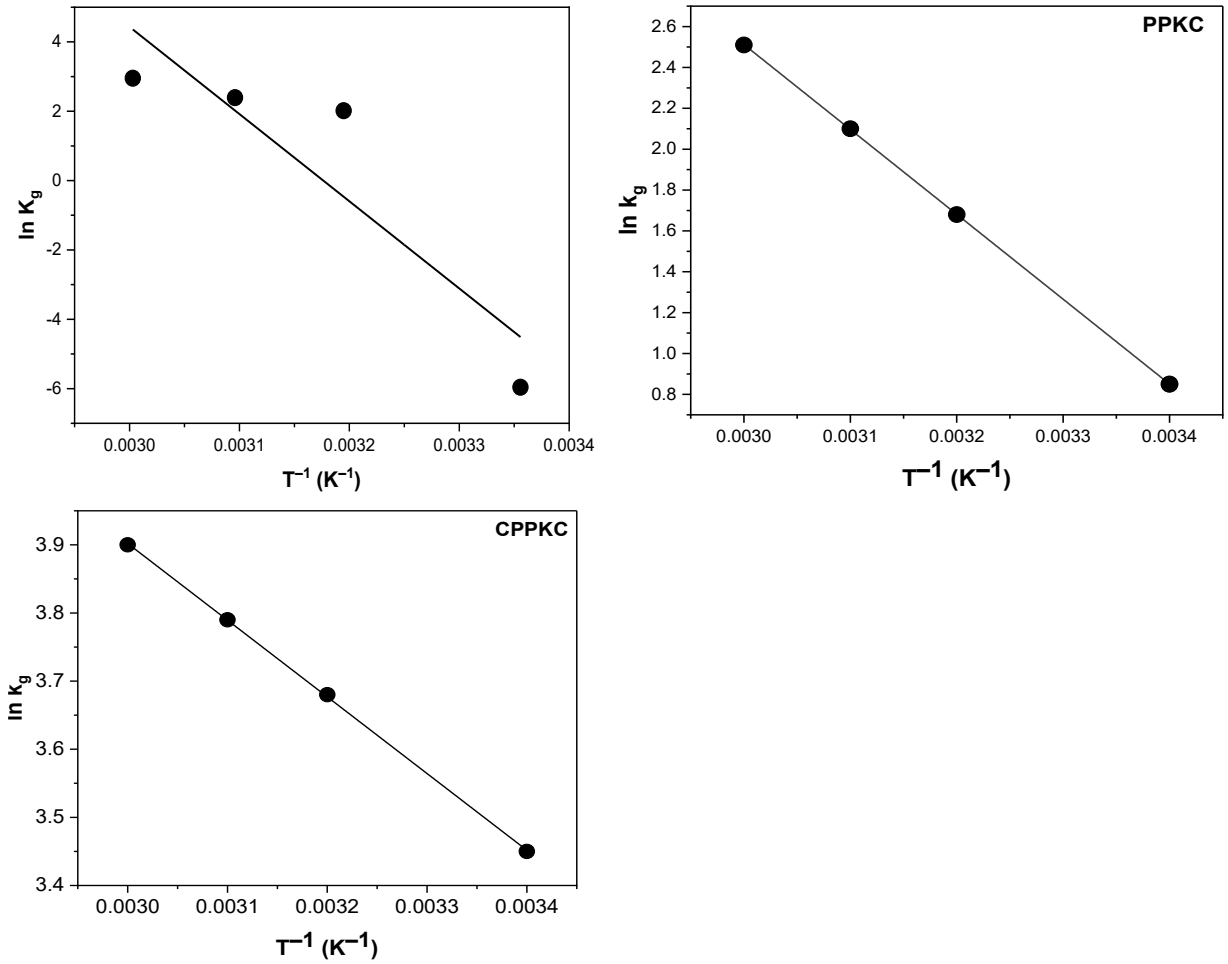


Figure 10: Vant-Hoff's plots for adsorption of Pb^{2+} onto RPKC, PPKC and CPPKC

4. Conclusion

The study has shown that physical pyrolysis followed by activation with phosphoric acid (H3PO4) on palm kernel chaff has converted the raw lingo-cellulosic substance to a very effective adsorbent (CPPKC) for the removal of Pb^{2+} ions from water. FTIR analysis showed that thermal and chemical modifications enabled the doping of nitrogen and phosphorus and increased the oxygenated functional groups such as O−H stretching and C=O stretching for better adsorption. SEM-EDX showed improved porous structure with sponge-like surface and higher oxygen content for better adsorption. Similarly, the thermo-gravimetric analysis (TGA) confirms the improved thermal stability (30.97% carbon) which has improved the properties, structure, and adsorption capacity of CPPKC. The adsorbent CPPKC exhibited the maximum

BET surface area of 116.13 m^2/g, pore volume of 1.4327 cm^3/g and pore diameter of 2.3752 nm. XRD patterns show amorphous arrangement in the modified biochars and crystalline arrangement in the raw adsorbent. The pH, adsorbent amount, time and initial concentration of lead (II) ions had a significant effect on the adsorption mechanism. The adsorption mechanism followed an Avrami fractional order model with improved capacity. The Liu model was the best isotherm model to describe the equilibrium data with the maximum capacity of 6131.7 mg/g at 50°C for CPPKC. Except RPKC, the lead(II) ions were spontaneously adsorbed on the adsorbents at 25°C. All the adsorbents showed an endothermic process of adsorption. The study points out that agricultural waste or by-products can be converted to low-cost, efficient and sustainable adsorbents for wastewater treatment, following the principles of circular economy.

Availability of Data

Data will be made available from the corresponding author on reasonable request.

Conflict of interest

No competing interests declared.

Ethical Approval

No human or animal study is involved by the authors.

Declaration of generative AI use

The authors declare that this article was prepared without the use of generative AI technologies.

Funding Declaration

No funding received.

Author contributions

All authors contributed to the study conception of this research. Conceptualization: [Idowu J. Esho, Emmanuel F. Olasehinde and Matthew A. Adebayo]; Methodology: [Idowu J. Esho]; Formal analysis and investigation: [Idowu J. Esho, Emmanuel F. Olasehinde and Matthew A. Adebayo]; Writing - original

draft preparation: [Idowu J. Esho and Matthew A. Adebayo]; Writing - review and editing: [Idowu J. Esho, Emmanuel F. Olasehinde and Matthew A. Adebayo]; Supervision: [Emmanuel F. Olasehinde and Matthew A. Adebayo]

References

Abbasizadeh S., Keshtkar A. R., Mousavian M. A. (2014). Sorption of heavy metal ions from aqueous solution by a novel cast PVA/TiO2 nanohybrid adsorbent functionalized with amine groups. *J. Ind. Eng. Chem.,* 20(4):1656–1664.

Adebayo M. A., Adediji J. F., Adebayo A. A. and Adebayo O. T. (2012). Equilibrium, kinetic and thermodynamic parameters of the biosorption of Ni^{2+} from aqueous solution by *Streblus asper*. Journal of Applied Sciences, 12(1): 71–77.

Adriana G., Marcela R., Nelly L., Patricia B., Guadalupe M., Brenda C., Eugenia C. M., Martha U., Isabel G., and Fortoul T. I. (2025). Lead systemic toxicity: a persistent problem for health. *Toxicology*, 154163. https://doi.org/10.1016/j.tox.2025.154163.

Ahsan M. A., Islam T., Hernandez C., Castro E., Katla S. K., Kim H., Lin Y., Curry M. L., Gardea-Torresdey J., Noveron J. C., 2018. Biomass conversion of saw dust to a functionalized carbonaceous material for the removal of tetracycline, Sulfamethoxazole and Bisphenol A from water. *J. Environ. Chem. Eng.*, 6, 4329–4338.

Aiyesanmi A. F., Adebayo M. A. and Arowojobe, Y. (2020). Biosorption of Lead and Cadmium from Aqueous Solution in Single and Binary Systems Using Avocado Pear Exocarp: Effects of Competing Ions. *Analytical Letters,* 53:18, 2868-2885, https://doi.org/10.1080/00032719.2020.1760294

Aiyesanmi A. F., Adebayo M. A. and Fadairo F. F. (2022). Evaluation of avocado pear seed coat for removal of nickel and chromium ions from aqueous solution. Journal of Hazardous, Toxic, and Radioactive Waste, 26(4): 04022027. https://doi.org/10.1016/10.1061/(ASCE)HZ.2153-5515.0000713

Alawa, B., Singh, S., Chakma, S., Kishor, R., Stålsby Lundborg, C., and Diwan, V. (2025). Development of novel biochar adsorbent using agricultural waste biomass for enhanced removal of ciprofloxacin from water: Insights into the isotherm, kinetics, and thermodynamic analysis. *Chemosphere, 375*, 144252.

Alejandro M. N., Martí, V., Sánchez-Hervás, J. M., and Ortiz, I. (2025). Development of Pistachio Shell-Based Bio-adsorbents Through Pyrolysis for CO_2 Capture and H_2S Removal. *Molecules*, *30*(7), 1501. https://doi.org/10.3390/molecules30071501.

Almanassra, I. W., Mckay, G., Kochkodan, V., Atieh, M.A., and Al-Ansari, T.A. (2021). A state of the art review on phosphate removal from water by biochars. *Chemical Engineering Journal, 409*, 128211. https://doi.org/10.1016/j.cej.2020.128211.

Amit A., Kumar V., Pandita S., Singh S., Bhardwaj R., Varol M., and Rodrigo-Comino J., 2023. A global meta-analysis of toxic metals in continental surface water bodies. *Journal of Environmental Chemical Engineering*. https://doi.org/10.1016/j.jece.2023.109964.

Arowojobe, Y., Aiyesanmi, A.F. and Adebayo, M.A. (2021). Removal of aqueous lead and cadmium using Persea americana seed coat: Single and binary studies. Advanced Journal of Chemistry: B, 3(1): 16–24. https://doi.org/10.1016/10.22034/ajcb.2020.243263.1057.

Ashkan M. F., 2023. Lead: Natural Occurrence, Toxicity to Organisms and Bioremediation by Lead-degrading Bacteria: A Comprehensive Review. *J Pure Appl Microbiol.* 17(3):1298-1319. doi: 10.22207/JPAM.17.3.26.

Ayach J., El Malti W., Duma L., Lalevée J., Al Ajami M., Hamad H., Hijazi A., 2024. Comparing Conventional and Advanced Approaches for Heavy Metal Removal in Wastewater Treatment: An In-Depth Review Emphasizing Filter-Based Strategies. *Polymers*, 16, 1959. https://doi.org/10.3390/ polym16141959.

Barakat, N. A. M., Mahmoud M. S., and Moustafa H. M., 2024. Comparing specific capacitance in rice husk-derived activated carbon through phosphoric acid and potassium hydroxide activation orfer variations. *Scientific reports,* 14, 1460. http://doi.org/10.1038/s41598-023-49675-0.

Benregga F. Z., Maghchiche A., Nasri R., Jraba A., 2021. Valorization of date seeds for preparation of bio activated carbon. *Journal of Fundamental and Applied Sciences,* 13(1), 292-309. doi: http://dx.doi.org/10.4314/jfas.v13i1.16.

BhagyaS., Kumari, S., Singh, S., Rani, I., Dhanda, A., and Chauhan, R. (2025). Exploring various types of biomass as adsorbents for heavy metal remediation: a review. *Environmental monitoring and assessment, 197 4*, 406. https://doi.org/10.1007/s10661-025-13826-9

Bondar A. N., 2022. Graphs of hydrogen bond networks to dissect protein conformational dynamics. The Journal of Physical Chemistry B., 126 (22), 3973-3984. https://doi.org/10.1021/acs.jpcb.2c00200.

Chakraborty, Ishita, Rongpipi, Sintu, Govindaraju, Indira, B, Rakesh, Mal, Sib Sankar, Gomez, Esther W., Gomez, Enrique D., Kalita, Ranjan Dutta, Nath, Yuthika, and Mazumder, Nirmal (2022). An insight into microscopy and analytical techniques for morphological, structural, chemical, and thermal characterization of cellulose. Microscopy Research and Technique, 85(5). https://doi.org/10.1002/jemt.24057.

Cheng, Y., Wang, B., Shen, J., Yan, P., Kang, J., Wang, W., Bi, L., Zhu, X., Li, Y., Wang, S., Shen, L., and Chen, Z. (2022). Preparation of novel N-doped biochar and its high adsorption capacity for atrazine based on π-π electron donor-acceptor interaction. *Journal of hazardous materials, 432,* 128757. https://doi.org/10.2139/ssrn.4010825.

Danso-Boateng, E., Mohammed, A. S., Sander, G. *et al.,* 2021. Production and characterisation of adsorbents synthesised by hydrothermal carbonisation of biomass wastes. *SN Appl. Sci.* 3, 257. https://doi.org/10.1007/s42452-021-04273-5.

Da-Silva B. F., Gonçalves J. O., Silva, L. F., Oliveira, M. L., Dotto, G. L., and Rhoden, C. R. (2025). Chitosan-based adsorbents for wastewater treatment: A comprehensive review. *International journal of biological macromolecules*, 143173. https://doi.org/10.1016/j.ijbiomac.2025.143173.

Dechapanya W., and Khamwichit A. (2023). Biosorption of aqueous Pb(II) by H_3PO_4-activated biochar prepared from palm kernel shells (PKS). *Heliyon,* 9(7), e17250. https://doi.org/10.1016/j.heliyon.2023.e17250.

El-Dein, W. A., Mahdi, Z. A., and Lotfy, H. R. (2025). A comprehensive study on pomegranate (Punicagranatum) peels as a low-cost biosorbent: adsorption mechanisms, application, regeneration, and cost analysis. *Environmental monitoring and assessment, 197 3*, 229. https://doi.org/10.1007/s10661-025-13626-1

Ewa S., Daniel G., Andrzej B., 2024. The significance of structural components of lignocellulosic biomass on volatile organic compounds presence on biochar-a review. *Wood science and Technology*, 58, 859-886. https://doi.org/10.1007/s00226-024-01557-y.

Fouda-Mbanga, B. G., Velempini T., Pillay K., and Tywabi-Ngeva Z. (2024). Heavy metals removals from wastewater and reuse of the metal loaded adsorbents in various applications: A review. *Hybrid Advances*. https://doi.org/10.1016/j.hybadv.2024.100193.

Gimba, C.E., J.Y., Olayemi, J. Y., Okunnu, S.T., and Kagbu. J. A., 2001. Adsorption of methylene blue by activated carbon from coconut shell. Global journal of Pure and Applied Sciences 7:265-268.

Hadi H. M., Ali M. S., Azil B. A., Ali H. J., Sami D. S., Deana Q., Mostafa M. M., Noah M. S., Mahmod A. A., 2024. Synthesis and Characterization of Xerogel Derived from Palm Kernel Shell Biochar and Comparison with Commercial Activated Carbon. *Journal of Ecological Engineering,* 25(6), 1–11 https://doi.org/10.12911/22998993/183719.

Isaac K. T., Ibrahim I., and Antonia Y. T., 2024. Recent advances in synthesis, characterization, and environmental applications of activated carbons and other carbon derivatives. *Carbon Trends,* 14, 100328, ISSN 2667-0569. https://doi.org/10.1016/j.cartre.2024.100328.

Jui-Yen L., Ingyu L., Jing-Hua T., Wanze L., Hyunook K., and Chin-Pao H., 2023. The surface acidity of freshly synthesized microplastics particles in simple electrolyte. *Colloids and surfaces A: Physicochemical and Engineering Aspects*, 675, 132000, ISSN 0927-7757. https://doi,org/10.1016/j.colsurfa.2023.132000.

Jun P., Ziyue Z., Ziwei W., Fang Z., Junxia Y., Ruan C., Chunqiao X., 2024. Adsorption of Pb2+ in solution by phosphate solubilizing microbially modified biochar loaded with Fe3O4. Journal of the Taiwan Istitute of Chemical Engineers, 156, 105363, ISSN 1876-1070. https://doi.org/10.1016/j.jtice.2024.105363.

Khandoker S. S., Nitesh Kumar K., Md. Ashiqur R., Hasan J., Youssef H., Stephen J. E., Alfred D. F., Lokendra P., and Lucian A. L., 2023. Comparison and assessment of methods for cellulose crystallinity determination. Chemical Society Review, 52 (18), 6417-6446. https://doi.org/10.1039/D2CS00569G.

Kolja J., Sheng W., Timo D., Tao S., Stefan H., Laihong S., and Maksym D., 2023. Characterizing devolatilized wood pellets for fluidized bed applications. *Biomass Conv. Bioref.* 13, 5133–5150. https://doi.org/10.1007/s13399-021-01486-x

Kuljit K., Rajandeep K., Harpreet K., 2024. A systematic review of lignocellusic biomass for remediation of environmental pollutants. Applied Surface ScienceAdvances, 19, 100547, ISSN 2666-5239. https://doi.org/10.1016/j.apsadv.2023.100547.

Kumar, P., Nashath O., S., Saravanan P., Rajeshkannan R., Rajasimman, M., Shanmugam, V., Kamyab H., Gupta V. K., and Vasseghian, Y. (2024). Exploring the role of activated charcoal from lignocellulosic biomass wastes for environmental pollution control. *Journal of the Energy Institute*, 114, 101626. https://doi.org/10.1016/j.joei.2024.101626.

Kumari, S., Chowdhry, J., Kumar, M., and Chandra Garg, M. (2024). Zeolites in Wastewater Treatment: A Comprehensive Review on Scientometric Analysis, Adsorption Mechanisms, and Future Prospects. *Environmental research*, 119782. https://doi.org/10.1016/j.envres.2024.119782.

Kumari, S., Chowdhury, A., Khan, A.A., and Hussain, S. (2021). Controlled surface functionalization of Ni-S nanostructures for pH-responsive selective and superior pollutants adsorption. *Journal of hazardous materials, 415*, 125750. https://doi.org/10.1016/J.JHAZMAT.2021.125750

Liang, J., Li, C., Zhang, S., Mohamed, B.A., Wang, L., Xiang, J., Hu, S., Wang, Y., & Hu, X. (2023). Activation of poplar and spirulina with H3PO4: Marked influence of biological structures of the biomasses on evolution structure of activated carbon. *Fuel Processing Technology*. https://doi.org/10.1016/j.fuproc.2023.107986.

Lima, E.C., Adebayo, M.A. and Machado, F.M. (2015). Experimental Adsorption. In: Bergmann, C.P. and Machado, F.M. (Eds). Carbon Nanomaterials as Adsorbents for Environmental and Biological Applications. 1st ed. p. 71–84. Springer International Publishing, New York. DOI: 10.1007/978-3-319-18875-1_4

Liu, F., Niu, J., Chuan, X., and Zhao, Y. (2024). Nitrogen and phosphorus Co-doped porous carbon: Dopant, synthesis, performance enhancement mechanism and versatile applications. *Journal of Power Sources*. https://doi.org/10.1016/j.jpowsour.2024.234308.

Mahmoud, E. R. I., Aly, H. M., Hassan, N. A., Aljabri, A., Khan, A. L., & F. El-Labban, H. (2024). Enhanced Removal of Chlorpyrifos, Cu(II), Pb(II), and Iodine from Aqueous Solutions Using Ficus Nitida and Date Palm Biochars. *ChemEngineering*, *8*(5), 105. https://doi.org/10.3390/chemengineering8050105.

Mititelu M., Neacșu, S. M., Busnatu, Ș. S., Scafa-Udriște, A., Andronic, O., Lăcraru, A. E., Ioniță-Mîndrican, C., Lupuliasa, D., Negrei, C., and Olteanu, G. (2025). Assessing Heavy Metal Contamination in Food: Implications for Human Health and Environmental Safety. *Toxics, 13*. https://doi.org/10.3390/toxics13050333.

Mitra A., Chatterjee S., Kataki S., Rastogi R. P., and Gupta D. K. (2021). Bacterial tolerance strategies against lead toxicity and their relevance in bioremediation application. *Environmental Science and Pollution Research, 28*, 14271 - 14284. https://doi.org/10.1007/s11356-021-12583-9.

Naifar A., Oueslati K., Lima E. C., Aouaini, and Ben L. A., 2025. In-depth study Captopril adsorption on a biosourced sorbent: Statistical Physics Approach and Pure Characterization, with Modeling of Adsorption Isotherms, Energetic, and Steric Analysis. *Langmuir: the ACS Journal of Surfaces and Colloids*, 41(25), 16115-16127. https://doi.org/10.1021/acs.langmuir.5c01235.

Neme, I., Gonfa, G., and Masi, C. (2022). Activated carbon from biomass precursors using phosphoric acid: A review. Heliyon, 8, e11940. https://doi.org/10.1016/j.heliyon.2022.e11940.

Olasehinde E. F., Adegunloye A.V., Adebayo M. A. and Oshodi A. A. (2019). Cadmium (II) Adsorption from Aqueous Solutions Using Onion Skins. *Water Conservation Science and Engineering,* 4:175–185. https://doi.org/10.1007/s41101-019-00077-2.

Olasehinde E. F., Adegunloye A.V., Adebayo, M. A. and Oshodi, A.A. (2018). Sequestration of Aqueous Lead(II) Using Modified and Unmodified Red Onion Skin. *Analytical Letters,* 51:17, 2708-2730, https://doi.org/10.1080/00032719.2018.1448989

Onyancha B. R., Osagie A., U., Eghonghon U. K., Septya K. H., Darmokoesoemo H., Adelaja O. O., and Pal, K. (2022). Influence of magnetism-mediated potential recyclable adsorbent for heavy metal ions removal from aqueous solutions - An organized review. *Results in Chemistry*. https://doi.org/10.1016/j.rechem.2022.100452.

Pan J, Deng H, Du Z, Tian K, Zhang J., 2022. Design of nitrogen-phosphorus-doped biochar and its lead adsorption performance. *Environ Sci Pollut Res Int.*, (19):28984-28994. doi: 10.1007/s11356-021-17335-3.

Qing L., Yongyao D., Yujie L., Qing H., Huiqui W., and Xu F.,2024. Effects of pyrolysis temperatures on the structural properties of straw biochar and its adsorption of tris-(1-chloro-2-propyl) phosphate. *Sci Rep*, 14, 25711. https://doi.org/10.1038/s41598-024-77299-5.

Raj, K., Vora, T., Padmapriya, G., Lal, B., Devi, A., Sharma, R., Chahar, M., Sudhakar, L., Suman, R., and Nagraik, R. (2025). A comprehensive review of sustainable hydrogels from lignin for advanced wastewater solutions. *International journal of biological macromolecules*, 139963. https://doi.org/10.1016/j.ijbiomac.2025.139963.

Samaraweera, H., Palansooriya, K.N., Dissanayaka, P.D., Khan, A.H., Sillanpää, M., and Mlsna, T. (2023). Sustainable phosphate removal using Mg/Ca-modified biochar hybrids: Current trends and future outlooks. *Case Studies in Chemical and Environmental Engineering*. https://doi.org/10.1016/j.cscee.2023.100528.

Shafiee M., Abedi M. A., Abbasizadeh S., Sheshdeh R. K., Mousavi S. E., Shohani S. (2020). Effect of zeolite hydroxyl active site distribution on adsorption of Pb(II) and Ni(II) pollutants from water system by polymeric nanofibers. *Sep. Purif. Technol.,* 55:1994–2011. https://doi. org/10.1080/01496395.2019.1624572.

Shi, W., Lian, W., Tian, S., Gong, X., Yu, Q., Guo, Z., Zhang, X., Ma, B., Bian, R., Zheng, J., Cheng, K., and Pan, G. (2023). A review of agronomic and environmental properties of inorganic compounds in biochars. *Current Research in Environmental Sustainability*, 5. https://doi.org/10.1016/j.crsust.2023.100226.

Sobik-Szołtysek, J.; Wystalska, K.; Mali ´nska, K.; Meers, E., 2021. Influence of Pyrolysis Temperature on the Heavy Metal Sorption Capacity of Biochar from Poultry Manure. Materials, 14, 6566. https://doi.org/10.3390/ma14216566.

Tiwari M., Dirbeba M. J., Lehmusto J., Yrjas P., and Vinu R. (2024). Analytical and Applied Pyrolysis of Challenging Biomass Feedstocks: Effect of Pyrolysis Conditions on Product Yield and Composition. *Journal of Analytical and Applied Pyrolysis*. https://doi.org/10.1016/j.jaap.2024.106355.

Tong, C., Liu, X., Zhang, J., Tie, B., Lei, M., Wei, X., Ou, P., & Du, H. (2021). Silicate-modified oil tea camellia shell-derived biochar: A novel and cost-effective sorbent for cadmium removal. *Journal of Cleaner Production, 281,* 125390. https://doi.org/10.1016/j.jclepro.2020.125390.

Veer S., Ghufran A., Sonali V., Pinki K., Sanjay K. C., Sachchida N. R., Emanuel V., and Ashish K., 2024. Toxic heavy metal ions contamination in water and their sustainable reduction by eco-friendly methods: isotherms, thermodynamics and kinetics study. *Scientific Reports*, 14:7595. https://doi.org/10.1038/s41598-024-58061-3

Wang X., Wang X., Che W., Yan J., and Zhang Q., 2025. Adsorption of Cu(ii) and Pb(ii) in aqueous solution by biochar composites. ACS omega, 10(14), 1316-13828. https://doi.org/10.1021/acsomega.4c06837.

Wipawee D., and Attaso K., 2023. Biosorption of aqueous Pb (II) by H3PO4-activated biochar prepared from palmkernel shells (PKS). *Heliyon,* 9(7). http://doi.org/10.1016/j.heliyon.2023.e17250

Xie, J., Latif, J., Yang, K., Wang, Z., Zhu, L., Yang, H., Qin, J., Ni, Z., Jia, H., Xin, W., & Li, X. (2024). A state-of-art review on the redox activity of persistent free radicals in biochar. *Water research, 255*, 121516. https://doi.org/10.1016/j.watres.2024.121516.

Xing, H., Jiang, G., Xiong, J., Zhu, Z., Zhang, L., Chen, M., and Zhu, J. (2023). The structure evolution from intrinsic micro-nano skeleton of natural wood to hierarchical porous carbon. *Microporous and Mesoporous Materials*. https://doi.org/10.1016/j.micromeso.2023.112653.

Xu W., Jin Y., and Zeng G. (2024). Introduction of heavy metals contamination in the water and soil: a review on source, toxicity and remediation methods. *Green Chemistry Letters and Reviews,* 17(1). https://doi.org/10.1080/17518253.2024.2404235.

Yan Y., Jiangtao H., Jiangyang S., Zixuan P., Qidong W., and Rui Y., 2023. Capacity and Mechanisms of Pb(ii) and Cd(ii) Sorption on Five-based Biochars. Sustainability, 15(9), 7627. https://doi.org/10.3390/su15097627.

Yang L., Yuan Y., 2025. Functional group characteristics of coal treated with clean biomass surfactant via FTIR spectroscopy. *Sci Rep*, 15, 18676. https://doi.org/10.1038/s41598-025-03769-z

Yun X., Ma Y., Zheng H., Zhang Y., Cui B., and Xing B., 2022. Pb(ii) adsorption by biochar from co-pyrolysis of corn stalks and alkali-fused fly ash. Biochar, 4, 66. https://doi.org/10.1007/s42772-022-00189-4.

Zakaria M. R., Mohammad A. A. F., Yoshito A., Irmawati R., Mohd A. H., 2023. Production of biochar and activated carbon from oil palm biomass: Current status, prospects, and challenges. *Industrial Crops and Products,* Volume 199, 116767, ISSN 0926-6690. https://doi.org/10.1016/j.indcrop.2023.116767.

Zhang, X., Chen, Y., Wang, Q., and Sun, Y. (2025). Advances in heavy metal wastewater treatment with biochar adsorption. *Biofuels, Bioproducts and Biorefining*. https://doi.org/10.1002/bbb.2751

Zhang, Z., Xiao, J., and Zhong, Q. (2023). Structural evolution of porous carbon heteroatom doping under oxidant on supercapacitor performance. *Materials Today Chemistry*. https://doi.org/10.1016/j.mtchem.2023.101416

Zhu Y., Huo G., Yang W., Liu H., Zhang W., Cheng W., Yang H., Wang Z., Jin Y., and Zhao H. (2024). Catalytic pyrolysis of duckweed with phosphoric acid: Pyrolysis behavior and kinetics analysis. *Journal of Analytical and Applied Pyrolysis*. https://doi.org/10.1016/j.jaap.2024.106384.